Optimized thin film processing of sodium mixed oxy-sulfide-nitride glassy solid electrolytes for all-solid-state batteries

Madison Olson[a], Jacob Wheaton[a], Mary Okkema[a], Nicholas Oldham[a] and Steve W. Martin[a]*
[a]Department of Materials Science and Engineering, Iowa State University of Science and Technology, 2240 Hoover Hall, 528 Bissell Rd, Ames, IA 50011, United States
*Email: swmartin@iastate.edu

Abstract

$Na_4P_2S_{7-6x}O_{4.62x}N_{0.92x}$ (NaPSON) glassy solid electrolytes (GSEs) were prepared and tested for their electrochemical properties and processability into thin films. The x = 0.2 composition (NaPSON-2) was found to be highly conducting, non-crystallizable, largely stable against Na-metal and supports symmetric cell cycling up to >100 μA cm^{-2} without shorting and for these reasons was processed into thin films drawn to 50 μm and tested in symmetric and asymmetric cells. Measurements of the sodium ion conductivity using symmetric cells demonstrated that the conductivity of NaPSON-2 was unchanged by film forming. Galvanostatic cycling at 5 μA cm^{-2} of 1.3 mm NaPSON-2 showed stability over 450 hours, while cycling a 50 μm thin film showed a very slow growth in the resistance. Cyclic voltammetry and x-ray photoelectron spectroscopy of the NaPSON-2 thin film GSE revealed that it did not react with Na-metal at its surface, but rather in the bulk of the film, showing S, Na_2S, and Na_3P reaction products. The source of the surface stability was determined to be the preferential segregation of trigonally coordinated nitrogen. These low-cost and easily processed NaPSON GSEs provide a system of materials which could provide for significantly lower cost higher energy density grid-scale batteries.

Keywords: Mixed oxy-sulfide-nitride glass; Solid-state electrolyte; Sulfide electrolyte; Thin film processing; Thin film; Electrochemical properties

1. Introduction

Research into renewable energy resources has increased significantly due to the growing demand for energy along with the cumulative and damaging impacts of burning fossil fuels. Wind and solar energy are promising net-zero carbon energy harvesters to lower CO_2 emissions. However, the intermittent nature of these energy systems has created a push to develop safe, low-cost, highly energy dense energy storage systems.[1] Solid-state sodium batteries (SSSBs) are being actively considered as alternatives to mature lithium ion batteries (LIBs) to lower cost and to reduce the competition for earth-scarce lithium resources in preference for earth-abundant sodium resources. To this end, while high temperature sodium-sulfur and sodium-nickel chloride batteries are already on the market today, they suffer from high cost, high thermal heat load requirements, and catastrophic failure modes.[2-3] Even though these battery systems take advantage of low-cost, abundant sodium materials and are known to have high energy density and long lifetimes; they run at significantly higher temperatures, increasing operating costs and lowering safety.[3-5] For these reasons, many installations often chose to use lower-operating-cost grid-adapted LIBs systems, even at the expense of safety and environmental concerns.[6-7]

The push for SSSBs comes from the need to eliminate the use of flammable, organic liquid electrolytes (OLEs) and expensive materials like lithium and cobalt[8], while enabling the safe application of highly-energy dense Na-metal anodes.[9] Although there are still many problems to be solved with other components in a SSSB, the solid-state electrolyte (SSE) separator has been the most heavily researched in order to solve the many critical problems caused by the use of OLEs.[10-13]

Out of the many candidates for these SSEs, glassy solid electrolytes (GSEs) are promising materials as replacements for OLEs. As a universal solvent, glass acts as an excellent medium to

probe wide compositional spaces to develop an optimized SSE that can meet processing and performance needs.[14] Glass can also be processed into homogenous and monolithic thin films. These thin films resist dendrite growth and enable the use of high energy density Na-metal anodes.[14-15] Sulfide GSEs materials have been heavily researched as viable GSEs due to their high ionic conductivity.[14, 16-20] For example, our group has studied a series of comparable mixed oxy-sulfide GSEs in the series $Na_4P_2S_{7-x}O_x$ where their conduction mechanisms have already been reported.[21] However, many sulfide and even mixed oxy-sulfide (MOS) GSEs can be difficult to process, particularly to thin films, because of their poor chemical stability and rapid crystallization when heated above their softening points that is required to form them into thin films.[22-25]

In contrast, pure oxide and mixed oxy-nitride (MON) based GSEs show excellent chemical stability and the processing methods for oxide glasses are simple and well known.[26-27] Further, it is quite common for oxide glasses to be processed down to the 10s of μm thicknesses at large scale as seen in smartphone screens.[28] For example, the large-scale processability of the oxide-based GSE, $LiPO_3$, to thin films for applications as a SSE has already been demonstrated.[29] Despite the low lithium ionic conductivity of $LiPO_3$ at room temperature, ~1 x 10^{-9} $(\Omega cm)^{-1}$, it showed the electrochemical viability of a thin film GSE by maintaining a low interfacial resistance in contact with lithium metal.[29]

Here, we expand upon our initial work that leveraged the easy processability of the pure oxide GSE $LiPO_3$, and report on a new sodium ion conducting mixed oxy-sulfide-nitride (MOSN) phosphate GSE series that exhibits a unique balance between processability as measured by its resistance to crystallization when heated to above its glass transition temperature (T_g) and its electrochemical performance when assembled into symmetric and asymmetric cells. These MOSN GSEs have the full composition $(1\text{-}x)[2Na_2S + P_2S_5] + x[Na_2S + 2NaPO_{2.31}N_{0.46}]$ which is

equivalent to $Na_4P_2S_{7-6x}O_{4.62x}N_{0.92x}$, where $0 \leq x \leq 0.5$ (NaPSON). With the atomic level short-range order (SRO) structures and their thermal behaviors already reported,[30] these NaPSON GSEs were synthesized in order to explore an optimized and processable composition (x in the expression above) that meets the required metrics of SSEs compatible with Na-metal anodes. Although the conductivities of these MOSN GSEs are very good for sodium ion conducting GSEs, they are still relatively modest and in the range of 1 x 10^{-6} $(\Omega cm)^{-1}$ at room temperature, but these NaPSON GSEs exhibit excellent chemical and thermal stability enabling processing into thin films (10s μm) without any evidence of crystallization or phase separation. Additionally, these NaPSON GSEs show stable cycling at 25 °C over hundreds of hours. As such, these low-cost and easily processed NaPSON GSEs provide an entirely new materials system which could provide for significantly lower cost, yet higher energy density grid-scale batteries.

2. Experimental Methods

2.1 Materials Synthesis

5 g batches of melt quenched (MQ) $Na_4P_2S_{7-6x}O_{4.62x}N_{0.92x}$, $0 \leq x \leq 0.5$ (NaPSON) compositions, and, for comparison purposes, of MQ $Na_4P_2S_{7-6x'}O_{6x'}$, $0 \leq x' \leq 0.5$ (NaPSO) compositions, were prepared with a constant R-value = 4Na/2P = 2. Batches were prepared inside a N_2 atmosphere glovebox (< 5ppm O_2 and H_2O) using stoichiometric amounts of phosphorus pentasulfide (P_2S_5 98% Acros Organics), sodium sulfide (Na_2S 99.9% Alfa Aesar), and NaPON (for the NaPSON GSEs) or $NaPO_3$ (for the NaPSO GSEs). The Na_2S was heat treated prior to use at 650 °C for 15 minutes in a vitreous carbon crucible to expunge excess sulfur observed in the as-received material. $NaPO_3$ and NaPON were synthesized according to methods developed by De Souza *et al*.[31] For the synthesis of NaPON, a bulk sample of $NaPO_3$ glass, approximately ~10-12

g, was directly nitrided through ammonolysis using NH_3 (g) for 6 hours at 780 °C[31]. The reaction of NH_3 with $NaPO_3$ is given in the reaction below, **Equation 1**[31].

$$NaPO_3 + yNH_3 \rightarrow NaPO_{3-3y/2}N_y + \frac{3}{2}yH_2O \quad (1)$$

The weight loss due to this ammonolysis reaction which occurred over 6 hours at 780 °C was 4.52 wt.%. Following the methods of De Souza *et al.*,[31] the nitrogen to phosphorus ratio (N/P) was determined using **Equation 2** below to be 0.46,

$$N/P = y = \frac{(101.96)(0.0452)}{9.992} = 0.46 \quad (2)$$

where, 101.96 g mol^{-1} is the formula weight of $NaPO_3$, 0.0452 is the fractional mass loss, assumed to be H_2O according to reaction schema shown in **Equation 1**, achieved after the nitridation process, and 9.992 g mol^{-1} is the oxygen to nitrogen weight exchange ratio.[31] The N/P ratio could then be used to calculate the specific composition of NaPON using **Equation 3** below.

$$NaPO_{3-3/2(0.46)}N_{0.46} = NaPO_{2.31}N_{0.46} \quad (3)$$

The above N/P ratio was assumed as an average value for the entire bulk sample of the prepared NaPON, so the bulk sample was ground to a fine powder to ensure a homogonous distribution of nitrogen would be incorporated into each of the small batch compositions.

Stoichiometric amounts of all of the starting materials were then milled inside a stainless steel pot with a single stainless steel ball using a Spex 8000M Mixer/Mill at 1725 rpm for 5 minutes to obtain a homogenous, well-mixed powder. The glass batch was then melted twice for 15 minutes each at 580 °C inside a covered vitreous carbon crucible inside a horizontal tube furnace hermetically sealed to the side of the glove box; once to determine if there was any disadvantageous weight loss of the glass batch on melting after cooling to room temperature,

typically < 2 wt.%, and a second time to ensure a homogenous liquid was achieved before quenching between two brass plates.

The composition for drawing thin film was chosen to be x = 0.2, NaPSON-2, in the NaPSON series and corresponds to the composition ~$Na_4P_2S_{5.8}O_{0.92}N_{0.18}$. A large batch of 150 g of NaPSON-2 was prepared by combining small batches of ~10 g, with NaPON with slightly varying N/P ratios between 0.45-0.55. The 10 g glass cullet batches, after being prepared as stated above, were combined and melted together at 580 °C inside a vitreous carbon crucible in a large vertical tube furnace hermetically sealed to the top of a large glove box for ~1 hour to generate a homogenous liquid. The molten glass was then cast onto a preheated brass mold 25 cm x 7 cm x 0.5 cm held at 190 °C and annealed for 24 hours before cooling to room temperature at 0.5 °C min^{-1}. This MQ NaPSON-2 preform was then processed into a thin film, as described in section **2.3.**. The thicker (mm scale) MQ and drawn thin film (μm scale) glass samples were stored and handled in the inert atmosphere of a glove box, either Ar or N_2, with levels < 5 ppm O_2 and H_2O.

2.2. Differential Scanning Calorimetry and Determination of the Viscosity

Approximately 6-12 mg of the glasses were sealed in hermetic aluminum sample pans for differential scanning calorimetry (DSC) measurements using a TA Discovery 2500 DSC. The DSC was used to determine the necessary parameters in the Mauro-Yue-Ellison-Gupta-Allan (MYEGA) equation[32], that was used to model the temperature-dependent viscosity, $\eta(T)$. All measurements of the onset T_g for the MYEGA model equation were determined at the heating and cooling rates given in **Table S1** and cycled between 50 and 250 °C, approximately 100 °C below and above the T_g. Other compositions T_g's were measured at 20 °C min^{-1} with the onset crystallization or melting temperatures (T_c and T_m, respectively) determined from these same DSC scans when crystallization of the supercooled liquid occurred.

2.3. Thin-Film Processing of the GSE

The cast and annealed GSE preform was transferred in an airtight container to a custom-built draw tower located inside a separate N_2 glovebox (<0.01 ppm O_2 and <0.01 ppm H_2O). A schematic diagram of the draw tower is shown in **Figure 1A.** The draw tower design allows for the adjustment of five different variables to control the film drawing process: the preform feed speed, upper furnace temperature, lower furnace temperature, the tractor speed, and the gas flow rate into the upper furnace zone. In order to draw the thin films, the preform was lowered so that the bottom 4 cm of the GSE preform was located in the hot zone of the upper furnace. The upper zone of the furnace was heated from room temperature to 193 °C at 0.25 °C min^{-1} and left to equilibrate for 4 hours, while the lower furnace was set to 100 °C. The actual temperature of the lower furnace was often higher than the setpoint temperature due to heat flow from the upper furnace. Following the isothermal hold at 193 °C, the gas flow was started at 0.2 standard liters per minute (SLPM), while the preform was heated to 214 °C at a rate of 0.5 °C min^{-1}. Slow heating rates were utilized to limit thermal shock and prevent fracturing of the preform during heating and as such emphasize the importance of the resistance to crystallization that these specialized GSEs must exhibit. Once the film had started to be drawn, the preform feed rate speed was set to 0.001 m min^{-1}, while the tractor rollers below the furnace gripping and pulling on the thin film were set to 0.1 m min^{-1}. This process led to films ~50 μm thick and ~5 cm wide, as shown in **Figure 1B,** when steady-state film drawing was reached. Before steady-state was reached, thicker films were produced and were also tested. While an edge thickening effect was observed,[29] see **Figure 1B**, there was still a large center section of usable film that was used for further testing.

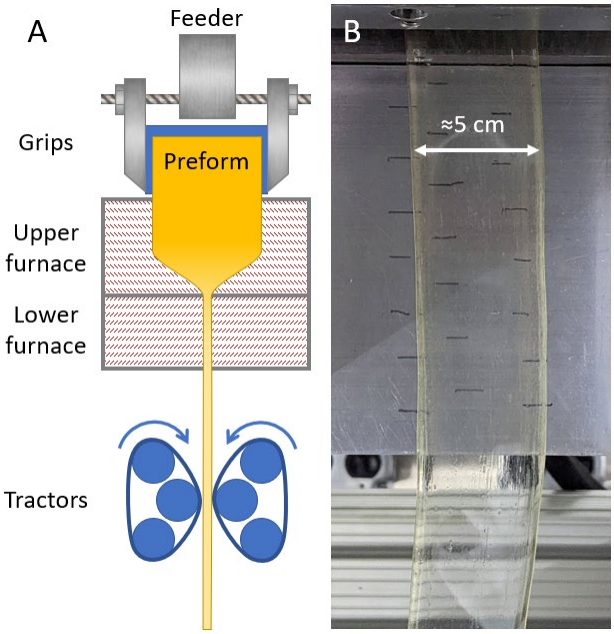

Figure 1: A) Side-view schematic of draw tower showing the main working features of the draw tower. **B)** Front-view image of a thin film as it exits the lower furnace before going into the tractor rollers.

2.4. Raman Spectroscopy

Pieces of MQ and drawn thin film glass were sealed under a N_2 atmosphere into a transparent tray and measured from 100 to 2000 cm^{-1} using an inVia 488 nm Renishaw Coherent Laser Raman Microspectrometer. Raman measurements were made to determine if the structure of the glass changed due to the thin film processing. Before collecting a Raman spectrum, the instrument was calibrated using an internal silicon reference standard centered at 520.5 cm^{-1} ($\pm$ 0.5 cm^{-1}). Each spectrum was collected using a 20x objective, 10 s exposure, and 12.5 mW power with a maximum of 20 accumulations per sample. Each sample was measured at least twice at different locations to ensure homogeneity of the sample.

2.5. Fourier Transform Infrared Spectroscopy

The MQ samples were prepared for Fourier transform infrared spectroscopy (FT-IR) by mixing the glass sample with cesium iodide (CsI) in a mass ratio of ~1:40, grinding the mixture

into a fine powder with a mortar and pestle, and pressing it into a thin pellet. The thin film samples were not diluted in CsI, because they were thin enough to allow direct testing in transmission mode through the thin film. Samples were transferred to the FT-IR in a sealed container and kept under constant N_2 flow until transferred to the vacuum chamber of the spectrometer. A Bruker IFS 66v/s FT-IR spectrometer was used to collect spectra under vacuum from 400 to 4000 cm^{-1} using a potassium bromide beam splitter. Measurements were obtained under vacuum with 4 cm^{-1} resolution and 32 accumulations.

2.6. Powder X-Ray Diffraction

X-ray diffraction (XRD) was run to ensure no crystallization occurred after thin film processing of the NaPSON-2 GSE. A sample of the thin film was ground to a powder and packed onto a zero-background silicon wafer, which was sealed in a Bruker air-tight sample holder. The XRD measurement was made using a Rigaku SmartLab X-ray Diffractometer from 20° to 90° 2θ with a step width of 0.01° and scan speed of 2° min^{-1} for a 45-minute scan duration.

2.7. Ionic and Electronic Conductivity

The temperature-dependent ionic conductivity of all the samples was measured using a Novocontrol 2 dielectric spectrometer equipped with a cryostat to determine the Arrhenius temperature dependence of the sodium ion conductivity, $\sigma_{d.c.}$, and its conductivity activation energy.

MQ GSE samples were prepared by casting and annealing the glass into a ~15 mm disk with a maximum thickness of ~2.5 mm. The samples were dry polished to ~1 μm grit and sputtered with gold electrodes (Au | GSE | Au), 10 mm in diameter, using an Anatech Hummer VI sputtering system. Each MQ sample was sealed in a custom air-tight sample holder. Samples were measured from -60 to 150 °C using a frequency range of 0.1 Hz to 10 MHz.

The ionic conductivity of the thin film GSE samples were made by constructing symmetric cells (Na | thin film | Na) in CR2032 coin cells. The thin film was not polished due to the mechanical fragility of the thin glass and because the surface of the thin film was smooth after the drawing process. The Na-metal electrodes were approximately 6 mm in diameter and placed on the thin film and MQ samples by hand. The stack pressure was no more than the pressure exerted by the coin cell, approximately 1 MPa. Due to the low melting temperature of Na-metal, ~98 °C, these samples were measured between -60 and 80 °C and compared to the conductivity of the MQ samples using the same frequency range of 0.1 Hz to 10 MHz.

Using a MQ sample and the same cell configuration for the MQ samples as described above (Au | GSE | Au), the electronic conductivity was determined by holding the GSE sample at various applied voltages for 9.5 hours and determining the limiting current. The applied voltage was set to 0.2 V and step-wise increased in increments of 0.2 V, with the maximum voltage being 1 V.

2.8. Electrochemical Characterization

Electrochemical characterization was done on the x = 0.2 NaPSON-2 GSE, in both MQ and thin film forms for comparison. Cyclic voltammetry (CV) measurements were done on asymmetric cells (Na | GSE | steel) while electrochemical impedance spectroscopy (EIS) and galvanostatic cycling experiments were done using symmetric cells (Na | GSE | Na) in CR2032 coin cells. The GSE was polished prior to cell assembly to ensure good contact between the Na-metal and steel electrodes for the symmetric and asymmetric cell configurations. The Na-metal electrodes were ~6 mm in diameter and placed on the GSE by hand. Again, the stack pressure was no more than the maximum pressure exerted by the coin cell. Measurements were made using a BioLogic VMP-300 potentiostat. EIS measurements were made immediately after cell assembly and then every 30 minutes to determine the evolution of the bulk and interfacial impedances over

a 24-hour period and to enable conformal contact of the Na-metal electrodes with the surface of the GSE before cycling.

2.9. X-Ray Photoelectron Spectroscopy

Samples were packed under an Ar atmosphere in an air-tight sample holder to transfer to the x-ray photoelectron spectroscopy (XPS) spectrometer. Sulfur (S2p), oxygen (O1s), nitrogen (N1s) and phosphorus (P2p) XPS were done on the NaPSON-2 thin film before and after CV and galvanostatic cycling at the surface and after Ar^+ ion etching. The post-CV and post-cycling coin cell samples were carefully opened using a crimping disassembler. The disassembly was done slowly to ensure the glass would not shatter due to the pressure of the de-crimping instrument. An area that was in contact with Na-metal was chosen for measurement in the XPS.

The XPS measurements were performed using a Kratos Amicus/ESCA 3400 instrument. The sample was irradiated with 240 W unmonochromated Al $K\alpha$ *x*-rays and photoelectrons emitted at 0° from the surface normal were energy analyzed using a DuPont-type analyzer. The pass energy was set at 150 eV. For sputter depth profiling, a beam of 500 eV Ar^+ ions was used. The emission current was 50 mA and the Ar partial pressure was 0.01 Pa. Under these sputtering conditions, the etch rate was ~1 nm s^{-1}. Two 300 second sputtering steps were performed to determine the depth profile. XPS data was fit with a Shirley baseline and a combination of Gaussian and Lorentzian line shapes.

3. Results and Discussion

3.1 Ionic Conductivity of MQ GSEs

The sodium ion conductivity for all GSEs in the NaPSON and NaPSO series was determined. **Figure 2A** shows a few of the Nyquist plots of the complex impedance of the NaPSON-2 MQ GSE for a few temperatures that were fit to obtain the effective d.c. impedances,

R_{bulk}, that were used to determine the d.c. sodium ion conductivity, $\sigma_{d.c.}$. The plots were fit according to the equivalent RC circuit model shown within **Figure 2B**, which includes a Warburg impedance that models the space-charge polarization of the mobile sodium ions in the vicinity of the blocking gold sputtered electrodes. The temperature-dependent ionic conductivities of the NaPSON GSE series are shown in **Figure 2B**. The Arrhenius dependence of the conductivities for NaPSO GSE series are given in **Figure S1** for comparison.

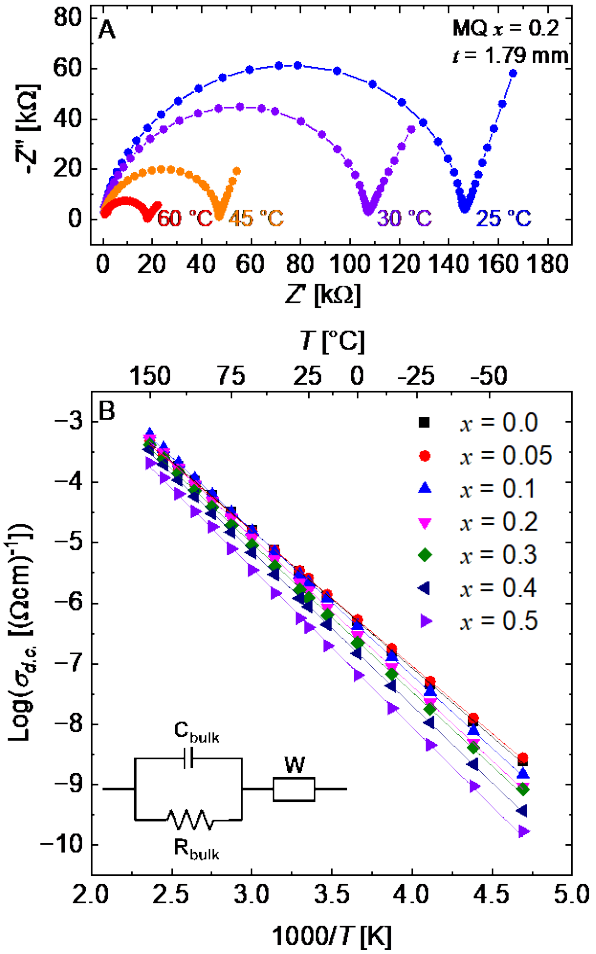

Figure 2: A) Nyquist plots of the complex impedance for the NaPSON-2 MQ GSE, sputtered with gold blocking electrodes (Au | GSE | Au) at 25, 30, 45 and 60 °C. **B)** Temperature-dependent ionic conductivity for all MQ GSEs in the $Na_4P_2S_{7-6x}O_{4.62x}N_{0.92x}$, $0 \leq x \leq 0.5$ glass series from -60 to 150 °C.

The Arrhenius plots for all x and x' GSEs were used to extract the activation energy, ΔE_{act}, of each composition in the NaPSON and NaPSO series as well as the conductivity at various temperatures, **Figure 3A,** using **Equation 4**.

$$\sigma(T) = \frac{\sigma_0}{T} \exp\left[\frac{-\Delta E_{act}}{RT}\right] \quad (4)$$

where ΔE_{act} can be divided into two terms, **Equation 5**:

$$\Delta E_{act} = \Delta E_c + \Delta E_s \quad (5)$$

and where the conductivity pre-exponential factor, σ_0, is given by the expression, **Equation 6**:

$$\sigma_0 = \frac{\omega_0 e^2 Z_c Z_a \lambda^2 n}{R} \quad (6)$$

In **Equation 5**, ΔE_C is the mobile carrier number activation energy and ΔE_S is strain activation energy. In **Equation 6**, ω_0 is the sodium ion vibrational frequency in its atomic energy well, e is the electron charge, Z_c and Z_a are the charges on the cation and anion, here +1 and -1, respectively, λ is the sodium ion jump distance between cation sites, n is the number density of sodium ions and R is the ideal gas constant.[33]

The conductivities at 0, 25, and 60 °C for both GSE series are shown in **Figure 3B** as a function of x and x'. With increasing x and x', which increases the oxygen content in the NaPSO series and the oxygen and nitrogen contents in the NaPSON system, respectively, there is a general decrease in the $\sigma_{d.c.}$ and a general increase in the ΔE_{act}. These trends are expected, and have been seen in literature in other MOS GSEs such as in Li_2O-Li_2S-P_2S_5 [23], $0.5Li_2S + 0.5GeS_{2-x}O_x$[34] and $Na_3PS_{4-x}O_x$ series[14] series, showing the same trend with additions of Li_2O in the former and oxygen in the two latter series, respectively. These results were interpreted as the higher field strength

oxygen anion creating deeper Coulombic energy wells, increasing ΔE_C, for the mobile lithium and sodium ions thereby increasing the total ΔE_{act}.[35]

However, on close inspection of **Figure 3A** for the x = 0.05 GSE, there is a significant decrease in the ΔE_{act} combined with a corresponding increase in the $\sigma_{d.c.}$ that is most apparent at low temperatures, 0 and 25 °C. Such an increase in the conductivity with small additions of oxygen to a pure sulfide GSE has been seen in the literature; for example, in the $0.5Li_2S + 0.5GeS_{2-x}O_x$[34] and the $Na_3PS_{4-x}O_x$ series.[14] The small decrease in the activation energy has been attributed to the incorporation of smaller anions, oxygen and nitrogen, which increases the free volume available for ion conduction at very low concentrations, thereby lowering the ΔE_S.[36] At x = 0.1, this effect on the volume becomes null as the smaller and higher field strength oxygen anion now decreases the free volume of the GSE which actually increases not only the mechanical ΔE_S but also the ΔE_C of the ΔE_{act}, thereby lowering the $\sigma_{d.c.}$ with further increases in x.[35-36]

When comparing the ion transport properties of the NaPSON and NaPSO GSEs, the decrease in the conductivity is found to be stronger with the additions of only oxygen with increasing x' in the MOS NaPSO GSE series, **Figure 3A** and **B,** compared to addition of oxygen and nitrogen to the MOSN NaPSON GSE series. This trend is expected, and found in literature, where any amount of nitrogen substituted for oxygen in any LiPON glass yields an increase in the ionic conductivity.[37] Here, small additions of nitrogen in the NaPSON GSEs, $x \leq 0.1$, do not have a strong effect on the $\sigma_{d.c.}$, but glasses with higher concentrations of nitrogen, $x \geq 0.2$, do have notably higher conductivities than the NaPSO GSEs.

The unexpected trend, however, appears in the activation energy, where although the conductivity is higher in the NaPSON glasses, so is the activation energy, compared to the NaPSO glasses. Consistent with the higher $\sigma_{d.c.}$ at a higher activation energy, the σ_0 values were found to

be larger in the NaPSON GSEs compared to those of the NaPSO GSEs, shown in **Table S2**, which gives numerical values for the conductivities at 0, 25, and 60 °C, and the ΔE_{act} and σ_0 values. Given the very similar composition and atomic level structures of the NaPSON and NaPSO GSEs, there are few parameters of σ_0 that are expected to be different between these two GSE series outside of n, the temperature dependent number density of charge carriers. **Equation 6** shows that n is thermally activated by ΔE_C. Given the relatively small differences in the conductivities of the NaPSO and NaPSON series, only modest decreases in ΔE_C are required to generate the increases observed. For example, comparing the glasses with the biggest difference in the conductivity, $x = x' = 0.5$, only a 1.5 kJ mol^{-1} decrease in ΔE_C accounts for this conductivity increase.

Similarly, research on nitrogen doped ionically conducting LiPON and NaPON GSEs have also reported higher conductivities over those of the pure oxide GSEs. These workers have associated the higher conductivities to the polarization of charge away from the charge compensating non-bridging oxygens (NBOs) by the higher field strength nitrogen.[37] This decrease in charge density at the NBO leads to a lower ΔE_C thereby increasing n for the NaPSON GSEs. So, despite the decrease in ΔE_C which increases n, the larger increase in ΔE_S increases the overall ΔE_{act}. However, these arguments do suggest that more research on this interesting behavior is needed to understand these compositional trends more fully.

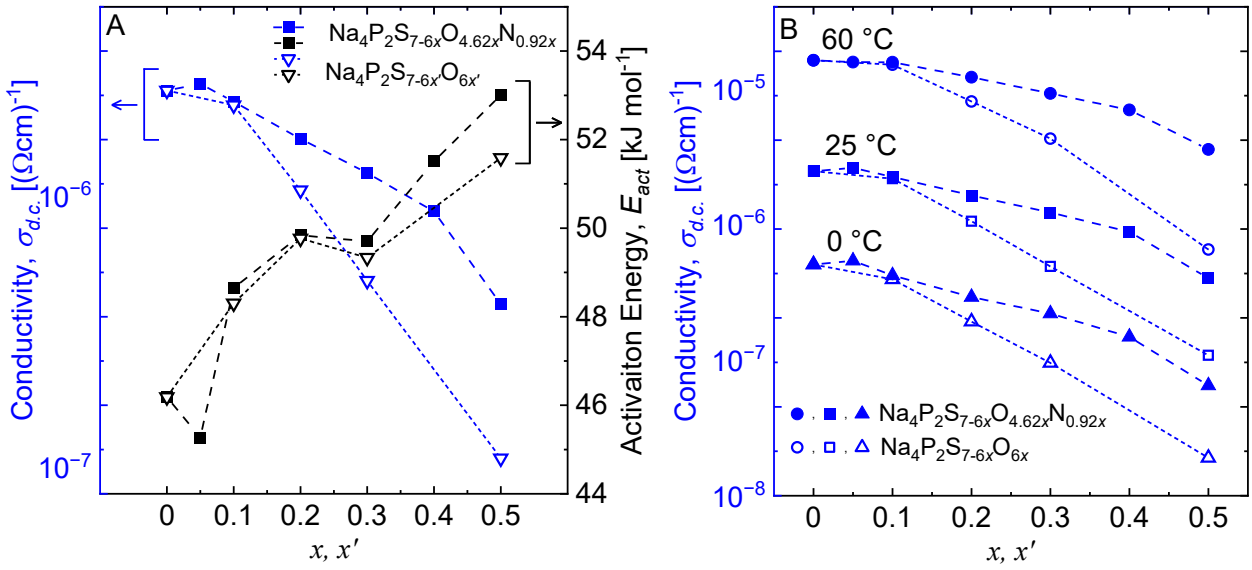

Figure 3: A) Conductivity at 25 °C and activation energy as well as the **B)** conductivity at 0, 25, and 60 °C for all x in the $Na_4P_2S_{7-6x}O_{4.62x}N_{0.92x}$ and $Na_4P_2S_{7-6x'}O_{6x'}$ glass series.

3.2 DSC and the MYEGA Model of the Viscosity

In determining an optimum composition for thin film drawing, resistance to crystallization and high ionic conductivity were initially considered as the most important criteria for compositional selection. To examine the crystallization resistance, the DSC thermograms of the x = 0.0, $Na_4P_2S_7$ (NaPS), x' = 0.2, NaPSO-2, and x = 0.2 NaPSON-2 GSEs are shown in **Figure 4**. Even though NaPS has the highest conductivity, it crystallizes only ~75 °C above its T_g and lacks the stability needed in the supercooled liquid state to resist crystallization during the slow heating steps used to draw thin films. Likewise, NaPSO-2, $Na_4P_2S_{5.8}O_{1.2}$, crystallizes ~100 °C above its T_g and is similarly unstable against crystallization in the supercooled liquid state.

However, **Figure 4** shows that the NaPSON-2, $Na_4P_2S_{5.8}O_{0.92}N_{0.18}$, does not exhibit any crystallization even when heated ~250 °C above its T_g and far into the supercooled liquid region. Indeed, an estimation of the liquidous temperature, T_l, given by the relationship $T_g/T_l = 2/3$,[38-39] is expected to be ~ 400 °C, meaning this liquid is resistant to crystallization across its full supercooled

liquid region, an incredible finding for these highly modified invert GSEs. Further, NaPSON-2 has a higher conductivity than NaPSO-2, which led it to be chosen for thin film forming.

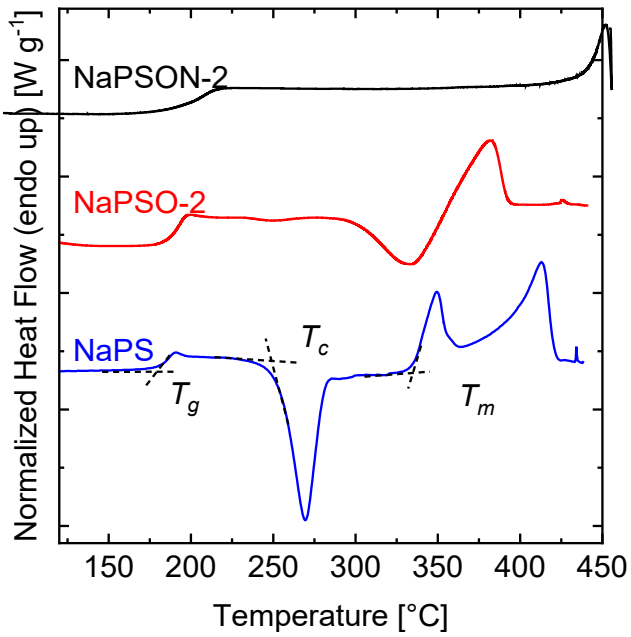

Figure 4: DSC thermograms for NaPS, NaPSO-2, and NaPSON-2 GSEs. DSC scans were run at 20 °C min^{-1} up to 450 °C.

In order to determine the processing temperature for viscous thin film drawing of NaPSON-2, the temperature dependence of the viscosity, $\eta(T)$, was modeled using the method of Mauro *et al.* and their MYEGA model[32] given in **Equation 7**.

$$\log_{10}\eta(T)=\log_{10}\eta_\infty+(12-\log_{10}\eta_\infty)\frac{T_{g10cpm}}{T}\exp\left[\left(\frac{m_{kin}}{12-\log_{10}\eta_\infty}-1\right)\left(\frac{T_{g10cpm}}{T}-1\right)\right] \quad (7)$$

In this model, only three parameters are necessary to determine $\eta(T)$, the infinite temperature viscosity, η_∞, the T_g at 10 °C min^{-1}, T_{g10cpm}, and the kinetic fragility index, m_{kin}. η_∞ was taken from literature values[40] as $10^{-0.5}$ Pa-s, while the T_{g10cpm} and m_{kin} were determined through DSC experiments. Following the methods by Mauro *et al.*[32], T_g was determined at varying heating rates, such that the previous cooling rate matches the following heating rate, **Table S1**, to establish

the same thermal history for each measurement of T_g, **Figure 5A**.[41] The T_g/T_{g10cpm} values were then plotted in an Arrhenius plot against the heating rate, $\dot{T}$, where the slope is the calorimetric fragility index, m_{cal}, **Figure 5B**. Finally, m_{cal} was converted to m_{kin} using **Equation 8**.[41]

$$m_{kin} = 1.289(m_{cal} - 14.97) + 14.97 = 94.5 \quad \textbf{(8)}$$

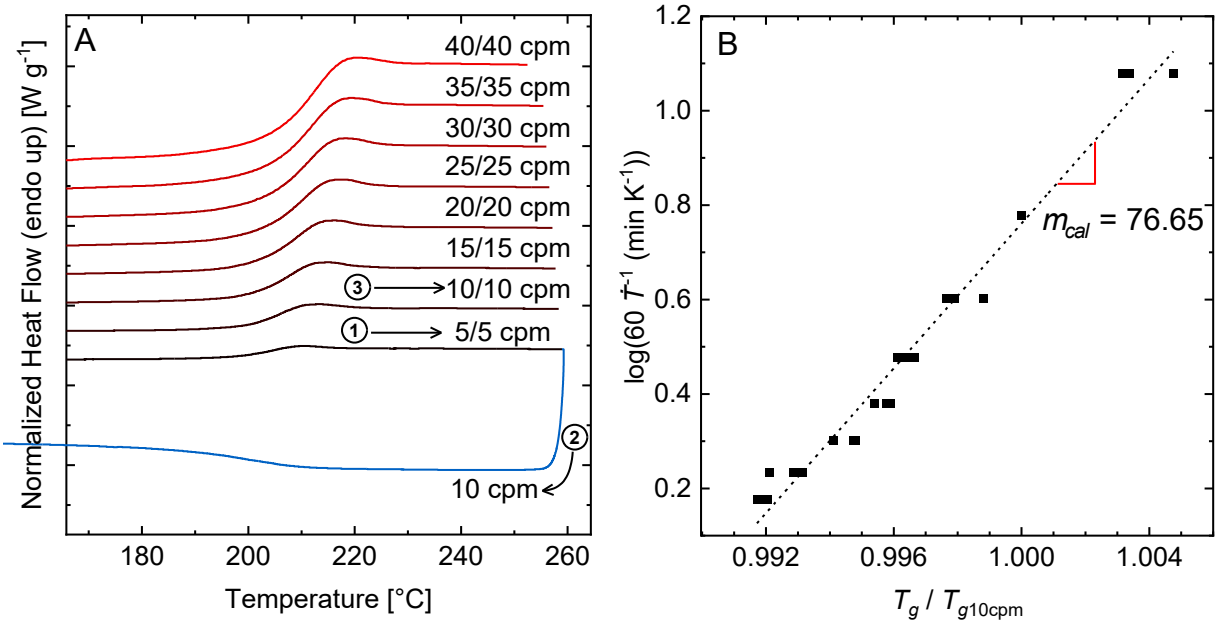

Figure 5: A) The DSC curves for NaPSON-2, run at equivalent cooling and heating rates as outlined in **Table S1**. The circled numbers show the progression of the heating and cooling scans used to determine the various T_g values. Note that NaPSON-2 is fully resistant to crystallization over all of these temperatures. **B)** Arrhenius plot of the heating rate and T_g/T_{g10cpm} values for three different NaPSON-2 samples run with the same program. The dotted line is a standard linear fit: the slope of which is the m_{cal}, representative of all three samples.

Using these three parameters, the $\eta(T)$ was calculated for NaPSON-2 using **Equation 7** and is shown in **Figure 6** which also shows the region of viscosities desired for thin film drawing of these GSEs. From the viscosity, it can be seen that the drawing temperature of 214 °C corresponds to a viscosity of ~$10^{9.5}$ Pa-s, significantly higher than the viscosity of ~ 10^4 Pa-s commonly reported for drawing oxide glasses.[42] This difference in draw viscosity could potentially

be due to differences in the draw speed. More work is being done to further explore the effects of temperature, draw speed and feed speed on the thin film drawing process.

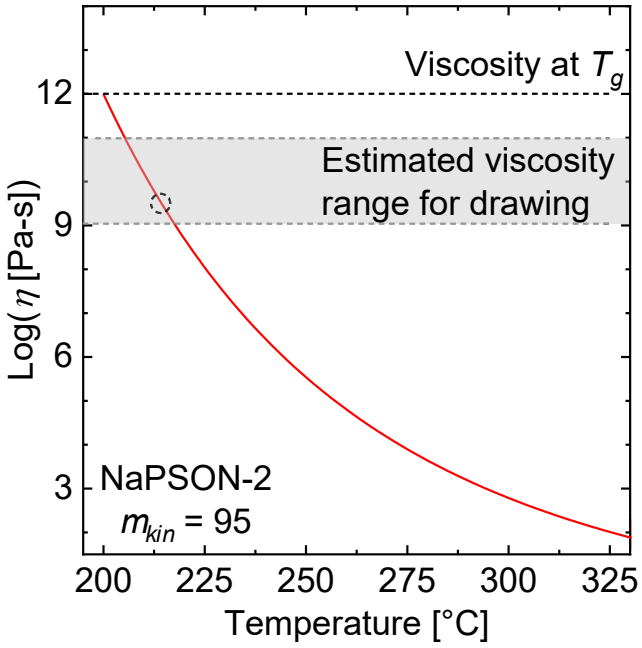

Figure 6: The temperature-dependent viscosity, $\eta(T)$, of NaPSON-2. The T_{g10cpm} value is the average from the three samples measured, 200 °C, and the m_{kin} is calculated using the slope in **Figure 5B**. The shaded red region denotes the error, calculated assuming a 95 % confidence of the slope in **Figure 5B**. The estimated viscosity range needed for drawing thin film (shaded in gray) and the actual temperature the film was drawn at (dotted circle) are shown.

3.3 Raman and FT-IR Spectra and Powder XRD

The Raman and FT-IR spectra of NaPSON-2 were used to determine if there were any significant chemical structural changes in the GSE during thin film processing, **Figure 7**. These spectra have already been used to carefully probe the SRO species in these NaPSO and NaPSON GSEs in bulk form and as such provided deep insight into the kind and proportion of each SRO species in these GSEs.[30, 43] The main peak in the Raman spectra centered at 400 cm^{-1} is attributed to the $P_2S_7^{4-}$ SRO unit, which has two shoulders at 387 cm^{-1} and 415 cm^{-1}, attributed to the $P_2S_6^{4-}$

and PS_4^{3-} SRO units, respectively.[44-45] The peaks between 450 and 550 cm^{-1} arise from vibrational modes associated with impurity level of ionic, $Na^+ {}^-S(S_n)S^-Na^+$, and covalent, S_n, sulfur species.[46-47] The FT-IR spectra shows the same pure sulfide SRO species as seen in the Raman spectra, where peaks centered at 560 cm^{-1} and 610 cm^{-1} are attributed to the non-bridging sulfur (NBS) of the PS_4^{3-} and $P_2S_7^{4-}$ anions, respectively.[46] The FT-IR spectra also show a mode centered at 463 cm^{-1} which is attributed to the dihedral bending of the bridging sulfur (BS), P-S-P, bonds and the asymmetric stretch of ionic sulfur, $^-S\text{-}(S_n)S^-$.[45-46] The modes centered at 878 cm^{-1} and 1043 cm^{-1} are attributed to the asymmetric vibration of bridging oxygens (BOs), P-O-P, bonds and the symmetric stretch of $P_2O_7^{4-}$ anions.[48] The other modes, centered at 936 cm^{-1}, 1091 cm^{-1}, 1156 cm^{-1}, and 1235 cm^{-1} are attributed to the NBO of PSO_3^{3-} anions, BO in P-O-P of $PO_{3.5}^{2-}$ units, and the symmetric stretch of O-P-O NBOs in PO_3^- and P=O in the PO_3^- anions, respectively.[48-49] Because the position, intensity, and area of each peak matches well between the MQ and thin film and there are no other peaks unique to either the MQ of thin film GSE, it is very likely that there is no significant structural changes in the glass after thin film processing.

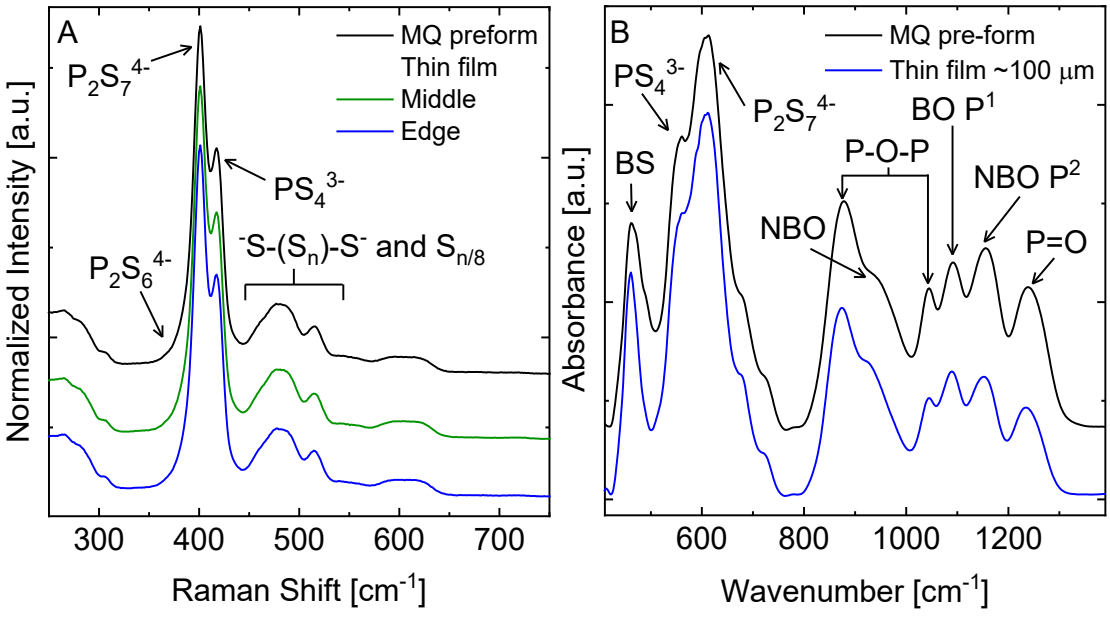

Figure 7: A) Raman spectra of the NaPSON-2 MQ preform and the thin film in the middle (~100 μm thick) and at the edge (~300 μm thick). **B)** FT-IR spectra of the MQ preform and a ~100 μm thin film.

In addition to examining the Raman and FT-IR spectra, powder XRD was used to verify that no crystallization occurred in the thin film during processing. The XRD pattern, **Figure S2**, shows no evidence of crystallization in the NaPSON-2 GSE thin film.

3.4.Sodium Ion Conductivity of Thin Film GSE

The Nyquist plots for a 50 μm thin film between 25 °C and 60 °C are shown in **Figure 8A**. These curves were fit using the same equivalent circuit used for the MQ GSEs, but without the Warburg impedance element, to determine their $\sigma_{d.c.}$. No polarization was observed in the Nyquist plot due to the use of non-blocking, Na-metal electrodes in the symmetric cells used to measure the samples. The ionic conductivities of thin films ranging in thicknesses between 50 μm to 250 μm were measured and compared to the conductivity of the MQ sample, **Figure 8B**. The $\sigma_{d.c.}$ values of each of the thin film samples shows good agreement to those of the MQ sample. The conductivity of the thin films at 25 °C varied between a maximum value of 2×10^{-6} $(\Omega cm)^{-1}$ and a minimum of 8.5×10^{-7} $(\Omega cm)^{-1}$. Recall, the MQ sample was measured with sputtered gold electrodes, while the thin film samples were measured using symmetric coin cells (Na | thin film | Na), and variations between the two measurements could be due to varying areas of the Na-metal electrodes. It can be concluded that the sodium ion conducting properties of the glass remain the same after processing.

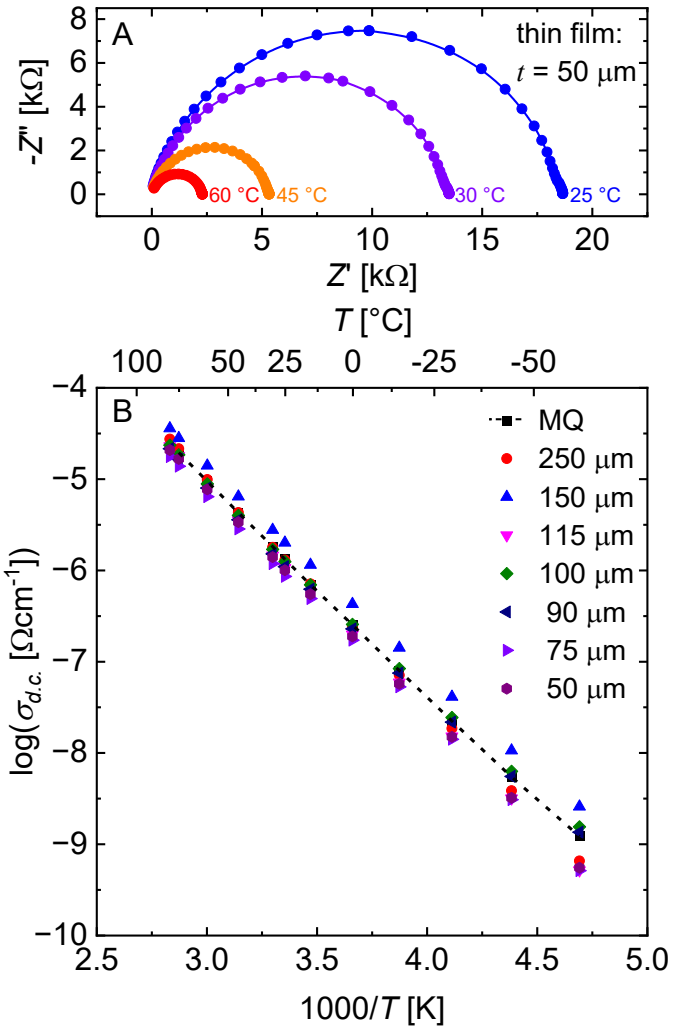

Figure 8: A) Nyquist plots of the complex impedance of a 50 µm NaPSON-2 GSE measured in symmetric coin cells (Na | thin film | Na) at 25, 30, 45 and 60 °C. **B)** Temperature-dependent ionic conductivity for the NaPSON-2 MQ sample, from **Figure 2B**, and over a range of thin film thicknesses from 50 µm to 250 µm. These samples were measured from -60 °C to 80 °C, to prevent the Na-metal electrodes from melting.

3.5. Electrochemical Characterization

3.5.1. Electrochemical Impedance Spectroscopy and Galvanostatic Cycling

While the thin film is the focus of this article, the MQ NaPSON-2 GSE was tested as a baseline for comparison to the thin film GSE. Before cycling, the bulk and interfacial resistances

as a function of time were determined for the MQ and thin film samples immediately after cell construction and then over 24 hours before cycling. The EIS and constant current cycling for the MQ NaPSON-2 GSE can be seen in the SI, **Figures S3 and S4**. **Figure 9A** shows EIS plots taken every 30 minutes to determine the evolution of the bulk and interfacial resistances after making the thin film cell. Then, the area specific resistances (ASRs) of the bulk and interface were determined and plotted as a function of time, **Figure 9B**. The NaPSON-2 50 μm drawn thin film showed a decrease in both the bulk and interfacial ASR values, **Figure 9**. This result was very similar for the MQ sample, **Figure S3**. In this cell, the initial bulk and interfacial resistances of the thin films are both higher prior to stabilizing after 24 hours. This is likely because during the assembly of the cell it is difficult to evenly press the Na-metal onto the surface of the thin film, because care has to be taken to not apply uneven pressure that might cause the thin film to fracture. This decrease in ASR has been attributed in other Na-metal-SE interfaces to void filling at the Na-GSE interface arising from the modest stack pressure applied by the coin cell that causes an increasing area with increasing time until the full area of the Na-metal electrode is filled in.[29, 50]

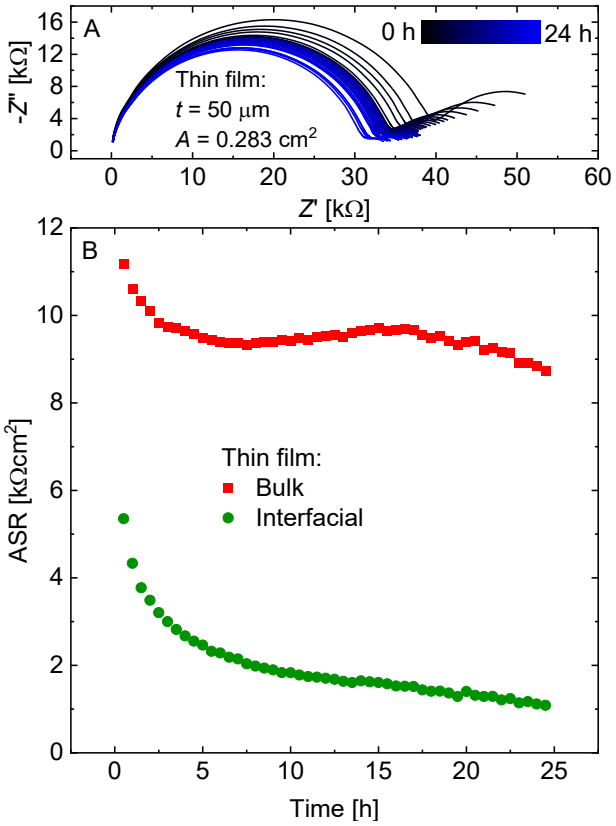

Figure 9: A) EIS measured after cell construction every 30 minutes for 24 hours on 50 μm thin film NaPSON-2 symmetric cell. **B)** The ASR of the bulk and interface plotted against time.

On the same symmetric cell, EIS measurements were made before and between each set of galvanostatic cycling experiments, **Figure 10,** at 5 μA cm^{-2} and room temperature on the NaPSON-2 50 μm thin film cell for 100 cycles. There was a definitive increase in the resistance, ~0.5% per hour, as seen in the increased measured voltage, over the cycling period of 450 hours. The resistance of the cell prior to cycling was ~36 kΩ, compared to 97 kΩ at the end of the last cycle. It is important to note that there was negligible change in the potential of the MQ sample after 450 hours of cycling, **Figure S4**. There were slight variations in voltage at each cycle as evidence of minor variation in the cell impedance over this series of cycles, but the changes seen are random and minor and perhaps associated with slight variations in temperature, **Figure S4**.

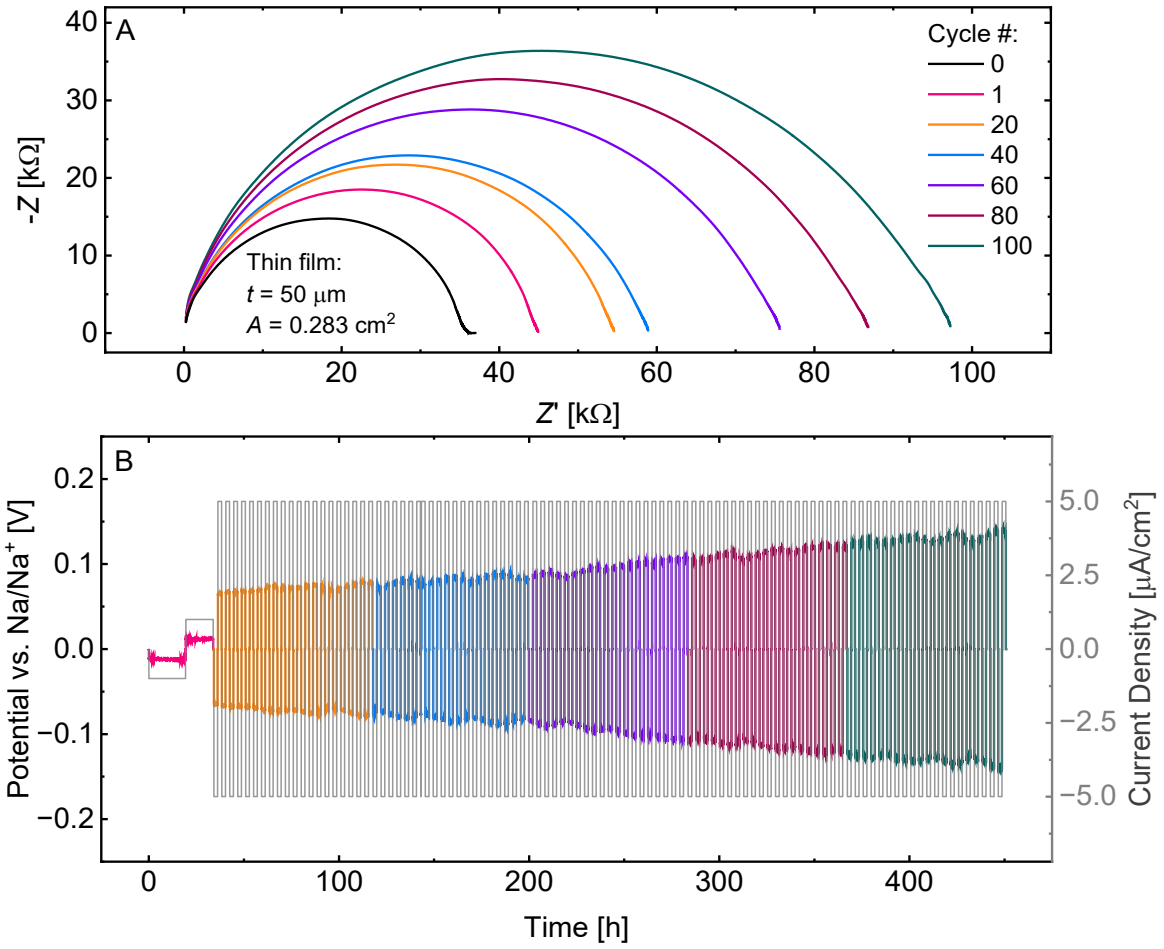

Figure 10: A) The EIS scans of a symmetric cell of a 50 μm thin film NaPSON-2 GSE run before, cycle 0, after one 40-hour cycle, cycle 1, then after each group of 20 cycles to determine the evolution of the cell impedance under an applied voltage and sustained current. **B)** Galvanostatic cycling over 450 hours. The first 35-hour cycle was run at 1 μA cm^{-2} to establish a conformal interface for further cycling at 5 μA cm^{-2} for 4-hour intervals.

After cycling for 450 hours, variable current density experiments were done on the same cells, starting at 5 μA cm^{-2} up to 100 μA cm^{-2}, **Figure 11**.

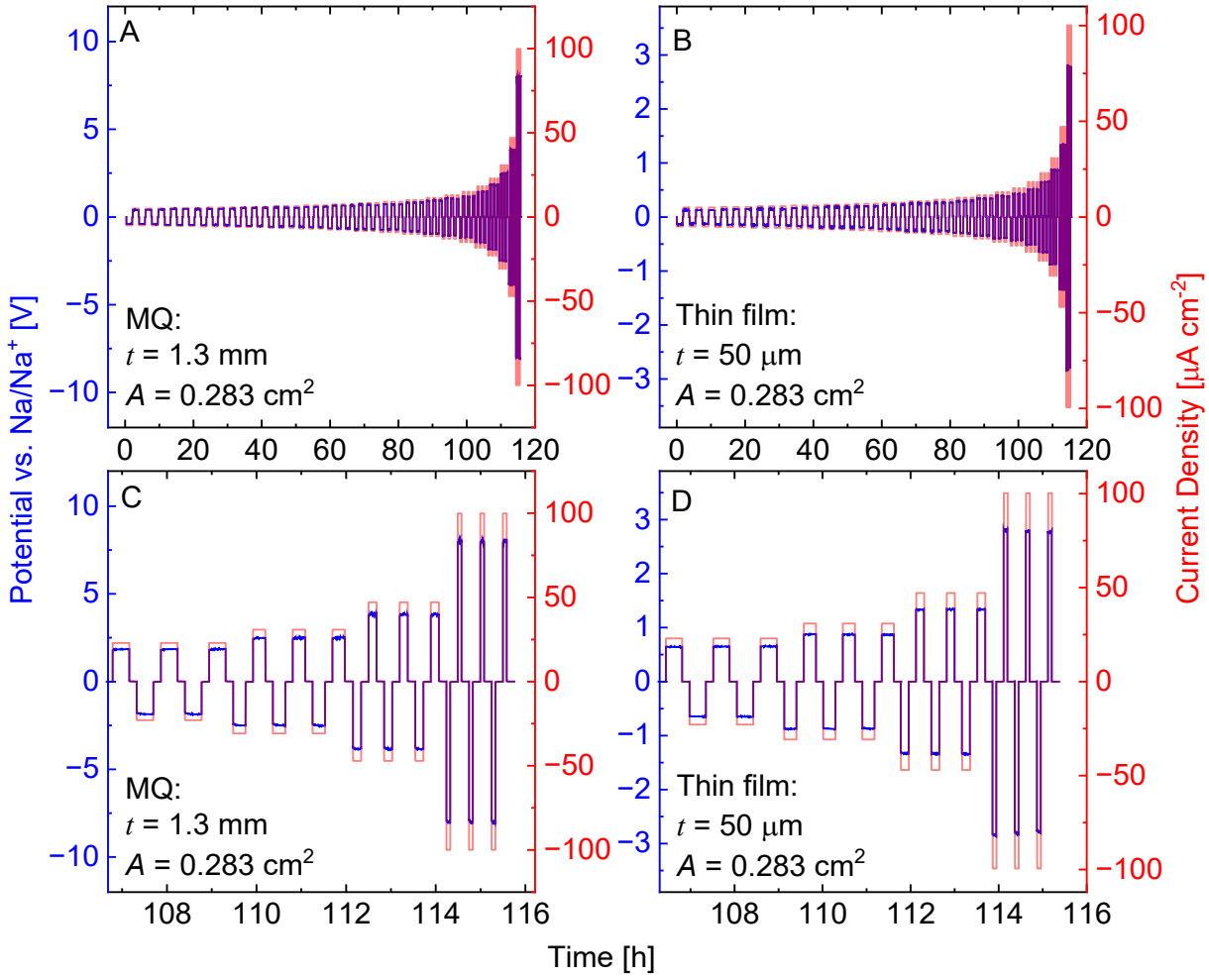

Figure 11: A-B) Variable current density experiments for the NaPSON-2 MQ and 50 μm thin film cells, respectively. Three cycles were run at each current density from 5 μA cm^{-2} to 100 μA cm^{-2}. **C-D)** Focused regions of the same graphs shown in **A** and **B**, respectively, for clarity.

Both the MQ, **Figure 11A and C**, and thin film cells, **Figure 11B and D**, sustained currents up to 100 μA cm^{-2} without shorting. However, the thin film cell showed a measurable increase in resistance after cycling for 450 hours, so any measured voltage for these variable current density experiments could be affected by this. Indeed, **Figure 11D** is consistent with a $\sigma_{d.c.}$ of 2 x 10^{-7} $(\Omega cm)^{-1}$ for the 100 μA cm^{-2} cycling data for the thin film, whereas **Figure 11C** is consistent with

an $\sigma_{d.c.}$ nearly a full order of magnitude higher at 1.7 x 10^{-6} $(\Omega cm)^{-1}$ for the MQ NaPSON-2 GSE. Despite the high current density achieved through the variable current density experiments, consistently cycling at these higher values proved challenging with the NaPSON-2 electrolyte. This is likely due to the reactivity, explained below, leading to poor cycling, and eventual shorting, see **Figure S5**.

3.5.2. Cyclic Voltammetry

To determine the oxidative stability of the NaPSON-2 MQ and thin film GSEs, asymmetric cells were assembled and used for CV scans. CV scans were run at 0.1 mV s^{-1} between -0.5 and 4 V to show the plating and stripping behavior, **Figure 12**, and between 0-4 V to emphasize any parasitic oxidation and reduction reactions that occur at higher voltages, **Figure 12**. Despite differences in the galvanostatic symmetric cell cycling, both the MQ and thin film GSEs show essentially the same result; notably, a clear peak at ~3 V associated with the reaction of free sulfur in the glass. **Equations 9** and **10** show the standard potentials for the oxidation of Na-metal and the reduction of sulfur, respectively, and combining these two equations, **Equation 11**, shows that the reaction due to the formation of Na_2S in the electrolyte occurs at 2.27 V. The shift to ~3 V, as seen in **Figure 12**, can be attributed to not only kinetic polarizations but also thermodynamic solutions reasons. While the Na-metal in this reaction can be considered as nearly standard state sodium, the sulfur is presumably not pure, as it is dissolved in the glass and not at unit activity. Further, this result is consistent with the Raman spectra of **Figure 7A** in section **3.3.** that showed the presence of free sulfur and polysulfides in the MQ and thin film NaPSON-2 GSE.

$$Na \rightarrow Na^{+} + e^{-} \quad ; \quad U^{Na} = -2.713 \tag{9}$$

$$S + 2e^{-} \rightarrow S^{2-} \quad ; \quad U^{S} = -0.407 \tag{10}$$

$$2Na^{+} + S^{2-} \rightarrow Na_2S \quad ; \quad U^{Na} - U^{S} = -0.407 - (-2.719) = 2.27\ V \tag{11}$$

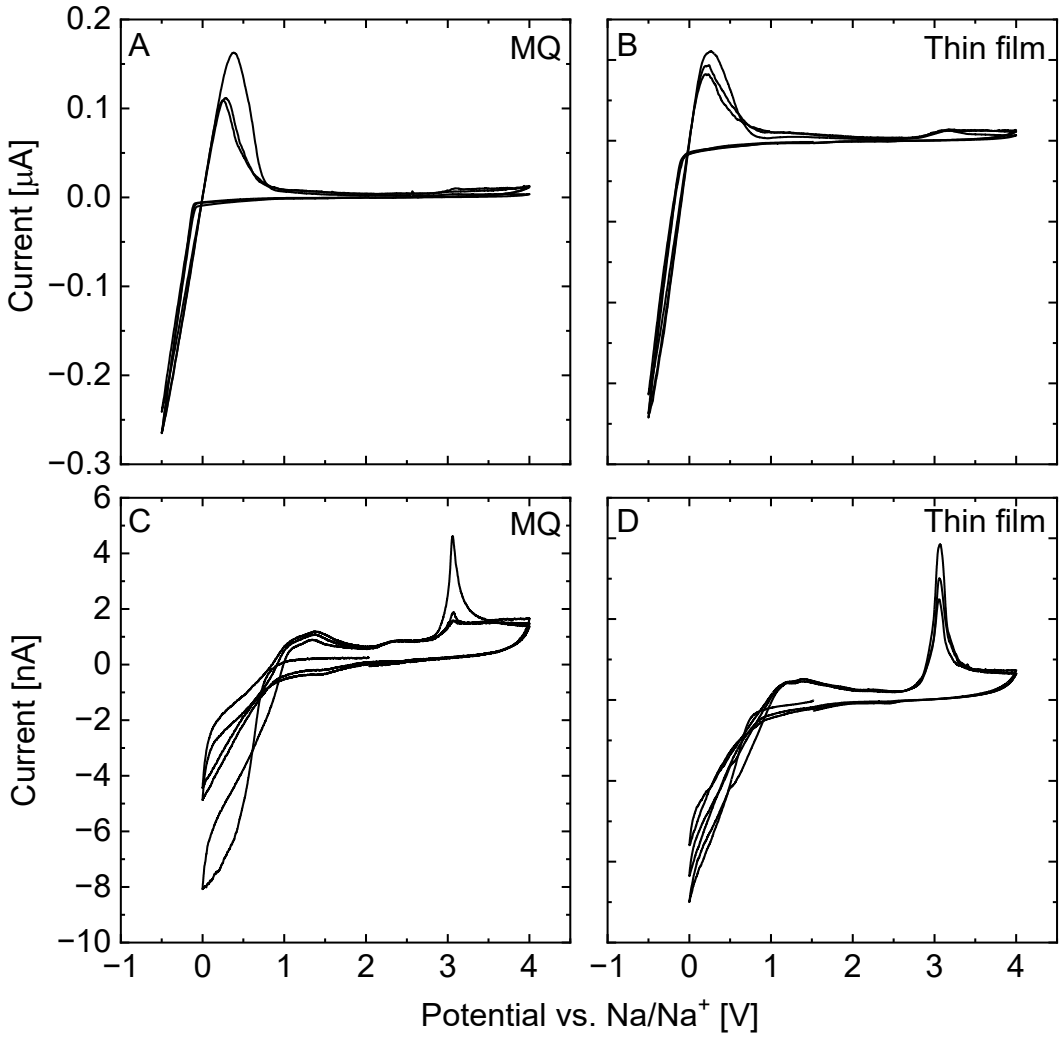

Figure 12: A-B) Wide voltage CV scan of NaPSON-2 measured between -0.5 to 4 V for the MQ and 700 μm thin film, respectively. **C-D)** Positive-only CV scan between 0 to 4 V to examine the reactions occurring in contact with Na-metal.

3.6. XPS of Reaction Products

Despite the similarities in structure and properties of the MQ and thin film NaPSON-2, there was a measurable increase in the resistance of the thin film. Significantly, the Nyquist plots shown in **Figure 10A** show no clear evidence of the formation of distinct interfacial impedance, rather a growth in bulk resistance. This suggests that it is the bulk of the thin film that is changing uniformly rather than an adlayer, meaning, that the instability of the NaPSON-2 thin film is not

limited to the interfacial contact with the Na-metal electrodes. To investigate this unusual behavior and the reaction observed through CV measurements, XPS was used to determine the oxidative stability and identify any decomposition reactions occurring, respectively.

Specifically, XPS was used to determine if the reaction products, Na_2S and sulfur that were suggested from the CV scans shown in section **3.5.2.**, were in fact present and if so to determine if they might be at root of the chemical changes leading to the increase in bulk resistance for the 50 μm thin film cell. S2p and P2p XPS are reported for the surface and Ar^+ ion etched depth of the pristine thin film and the Na-metal side of the post-mortem CV cell and symmetric 50 μm thin film cell. To illustrate differences in the surface and depth profiles of these samples, the O1s and N1s XPS are also reported.

3.6.1. Sulfur S2p XPS

The S2p XPS of the as-synthesized pristine thin film and the post-mortem CV and symmetric 50 μm thin film cells for the surface and depth are shown in **Figure 13**.

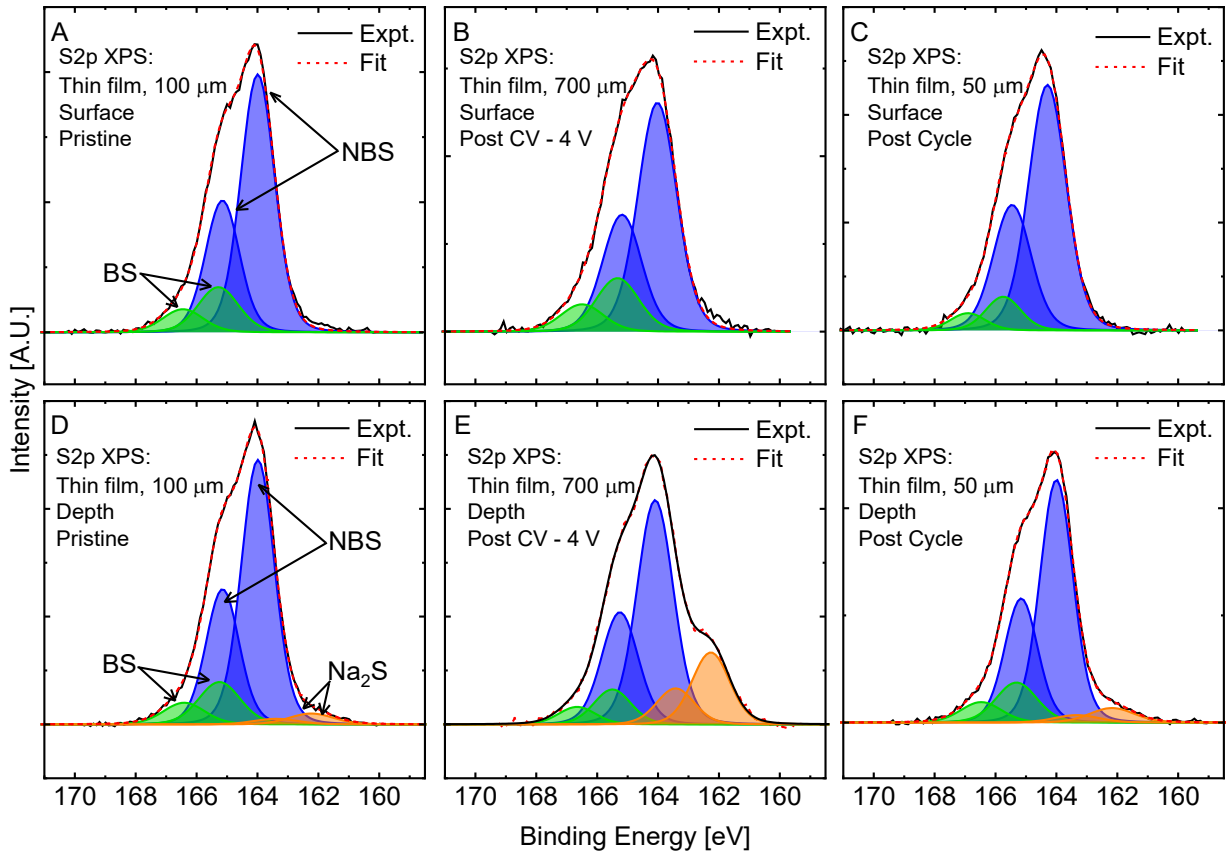

Figure 13: A-C) S2p XPS of NaPSON-2 GSE surface of the as-synthesized pristine thin film, post-mortem CV cell, and post-mortem 50 μm cell, respectively. **D-F)** S2p XPS of NaPSON-2 of the depth of the as-synthesized pristine thin film, post-mortem CV 700 μm cell, and post-mortem 50 μm cell, respectively. S2p XPS shows the formation of excess, impurity Na_2S formed in the bulk.

The results of the S2p XPS show the same chemical species at the surface, even for samples measured after contact with Na-metal in both asymmetric CV cells (**Figure 12**) and symmetric galvanostatic cycling cells (**Figure 10**), **Figure 13A-C**. The three spectra do show one set of peaks at higher binding energies that are centered at 167.3 eV and 166.0 eV, which have been assigned to the S2p1/2 and S2p3/2 spin-orbits of the BS species, respectively, and a second set of lower binding energy peaks centered at 165.2 eV and 164.0 eV, which have been assigned to the S2p1/2 and S2p3/2 spin orbits of the NBS species, as highlighted in **Figure 13A**.[51-52] Again, and significantly, the surfaces of the pristine thin film, the CV scanned thin film, and the galvanostatic

cycled thin film all show the same and expected constitution of the expected sulfur species and do not show any apparent changes in chemistry after exposure to and cycling in contact with Na-metal .

However, upon etching the surface, the exposed depth of the pristine thin film, **Figure 13D**, shows impurity peaks centered at 162.5 eV and 162.1 eV which are attributed to the S2p1/2 and S2p3/2 spin orbits of Na_2S.[53-54] The etched surface of the sodium side of the post-mortem CV cell, **Figure 13E**, shows a significant growth in these same peaks associated with Na_2S. Finally, the post-mortem 50 um cell, **Figure 13F**, shows a small but measurable increase in relative area of sulfur XPS peaks associated with increased concentrations of Na_2S compared to the pristine sample. These results are consistent with the CV results that suggest that the production of Na_2S occurs at 3 V vs. Na^+/Na.

3.6.2. Phosphorus P2p XPS

The P2p XPS of the pristine NaPSON-2 thin film and thin films from the post-mortem CV (**Figure 12**) and galvanostatic symmetric cells (**Figure 10**) collected from the surface and the Ar^+ ion etched depth are shown in **Figure 14**.

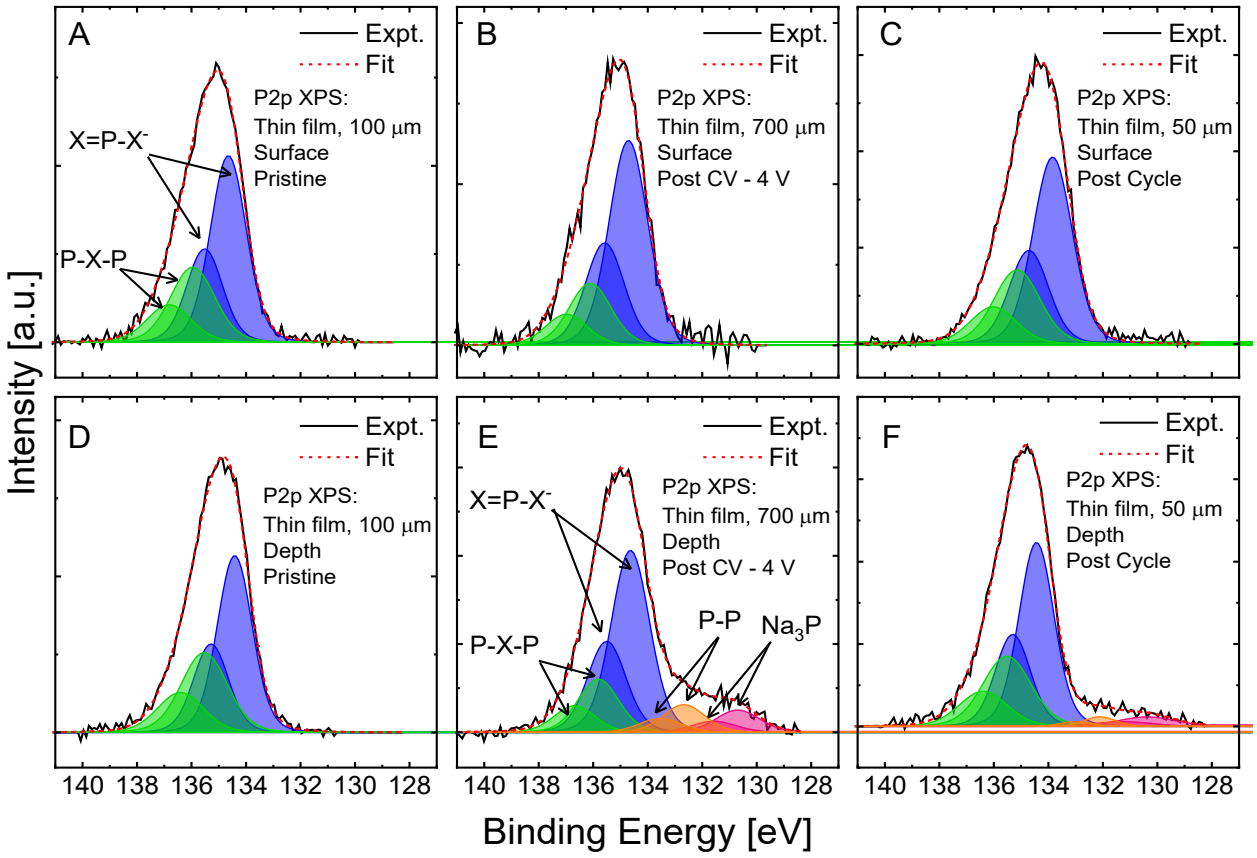

Figure 14: A-C) P2p XPS of NaPSON-2 of the surface of the as-synthesized pristine thin film, post-mortem CV cell, and post-mortem 50 μm cell, respectively. **D-F)** P2p XPS of NaPSON-2 of the depth of the as-synthesized pristine thin film, post-mortem CV 700 μm cell, and post-mortem 50 μm cell, respectively. P2p XPS shows the formation of the defect anion $P_2S_6^{4-}$ and Na_3P formed in the bulk under an applied voltage and sustained current.

Similarly to the S2p XPS, the P2p XPS of the surface scans for all of these samples are essentially identical and showed no evidence of impurities or reaction products as a consequence of testing, **Figure 14A-C**. **Figure 14A** shows the P2p XPS of the pristine thin film and the phosphorus chemical species, with peaks centered at 134.8 eV and 135.9 eV, are assigned to the P2p1/2 and P2p3/2 spin orbits of phosphorus atoms in non-bridging X=P-X$^-$ bonds (X = S, O, or N in these MOSN glasses), respectively.[55] The peaks centered at 136.9 eV and 138.2 eV are

attributed to the P2p1/2 and P2p3/2 spin orbits of the phosphorus atoms in bridging P-X-P bonds in the glass.[55]

Now, turning to the Ar^+ ion etched exposed depth of the as-synthesized thin films, **Figure 14D** shows the P2p XPS spectra of the pristine thin film is unchanged from that of the surfaces and shows no evidence for chemical impurities or reaction products. This is significant because as described in section **3.3.**, the Raman spectra, **Figure 7A**, shows that a small concentration of defect $P_2S_6^{4-}$ anions, which are missing the BS between the two phosphorus atoms, is present in the as-synthesized thin film due to the presence of the small shoulder at 387 cm^{-1}. To form $P_2S_6^{4-}$ anions, the BS in the P-S-P bond is removed from the $P_2S_7^{4-}$ anion, leaving phosphorus to bond with itself and excess free sulfur in the glass. The latter species is confirmed in the Raman spectra, **Figure 7A,** by the presence of a peak at ~ 472 cm^{-1}, associated with free sulfur. The absence of a P2p XPS signal arising from the P-P bond in this $P_2S_6^{4-}$ defect may suggest that its concentration is below the detection limit in the P2p XPS measurements of the pristine sample.

From the P2p XPS spectra of the thin film GSE from the post-mortem CV cell, **Figure 14E**, and the thin film post-mortem symmetric galvanostatic cycling cell, **Figure 14F**, there is evidence that reduced phosphorus species form based on the peaks at 133.6 eV and 132.7 eV which are assigned to the P2p1/2 and P2p3/2 of the $P_2S_6^{4-}$ defect anion. The presence of a second reduced phosphorus species is evidenced from the peaks at 130.7 eV and 131.6 eV and this peak is assigned to the P2p1/2 and P2p3/2 of sodium phosphide, Na_3P.[54-56] The XPS of Na_3P can be found in **Figure S6**.

In summary, the P2p XPS spectra combined with the S2p XPS spectra suggest that the reaction $P_2S_7^{4-} \rightarrow P_2S_6^{4-} + S$ occurs on symmetric cell and CV cycling, where the excess sulfur reacts with Na-metal and forms additional excess Na_2S in the GSE. In a similar way, it is suggested

that the PS_4^{3-} anion decomposes to form Na_3P and Na_2S.[57] Hence, the formation of Na_2S must be electrochemically and chemically favorable to form from the pure sulfide glass network species, PS_4^{3-} and $P_2S_7^{4-}$, at oxidizing potentials, **Figure 14E**, as seen in the CV scans, and to a lesser extent, **Figure 14F,** after galvanostatic cycling.

3.6.3. Oxygen (O1s) and Nitrogen (N1s) XPS

In addition to the S2p and P2p XPS, the O1s and N1s XPS spectra were also collected to determine if there were any differences in the chemistry between the surface and bulk of the thin films, which may be the cause of the increased electrochemical stability of the surface of the thin film. **Figure 15** shows that both the O1s and the N1s XPS show an observable difference between the surface and depth profile of the NaPSON-2 thin film.

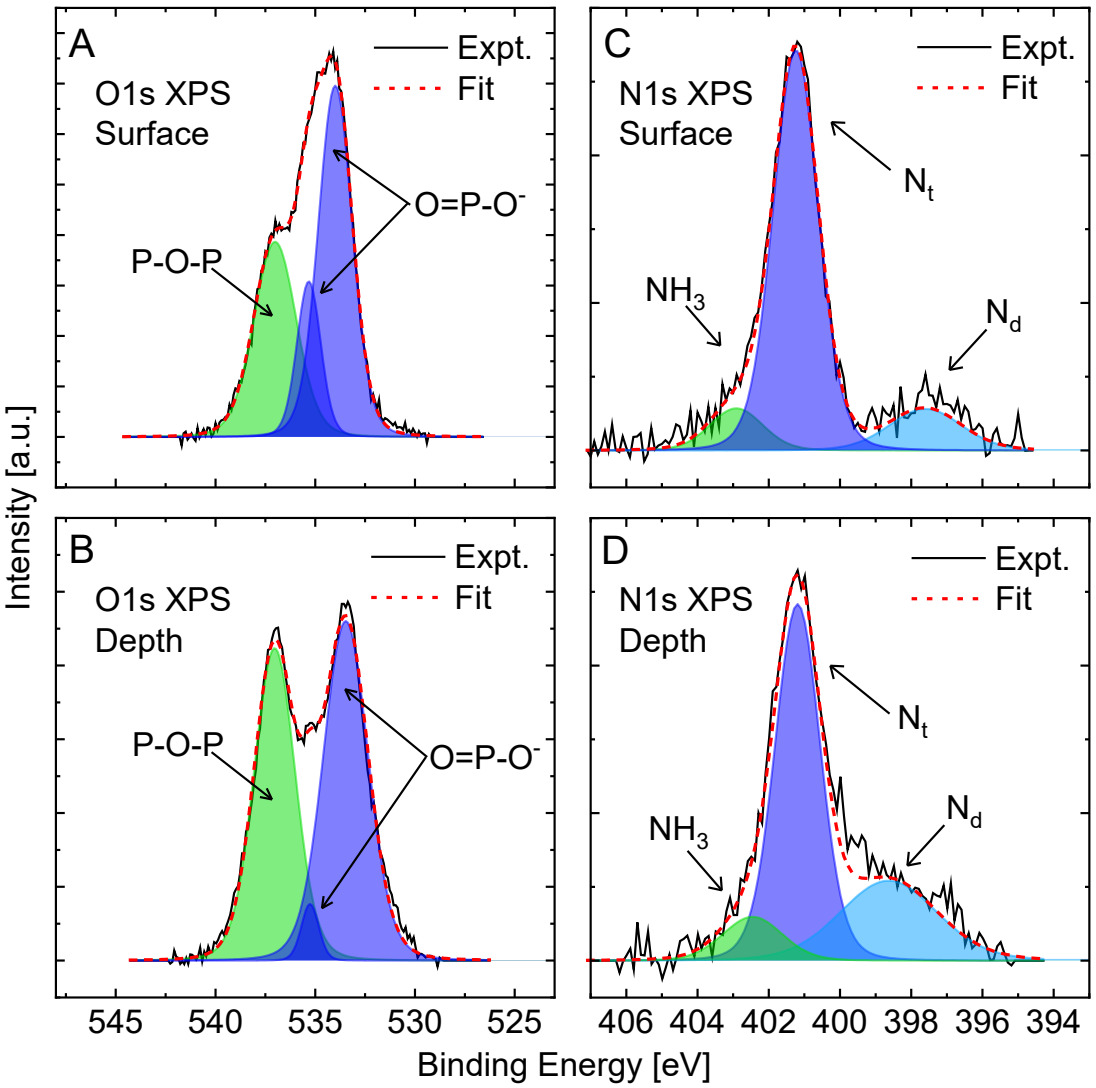

Figure 15: XPS spectra of pristine NaPSON-2 100 μm thin film. **A-B)** O1s XPS **C-D)** N1s XPS at the surface and depth. There is a greater concentration of N_t and NBO species at the surface compared to the depth.

The O1s XPS shows peaks centered at 537 eV, corresponding to the BO of the P-O-P bonds, and at 535 eV and 534 eV correspond to the two NBOs in the glass associated with the doubly bonded oxygen and the charged oxygen of the O=P-O$^-$ unit.[37, 58] The N1s XPS spectra shows peaks centered at 403 eV, 401.2, and 398 eV and are assigned to a minor impurity of NH_3, trigonal coordinated nitrogen (N_t) and linearly coordinated, doubly bonded nitrogen (N_d), respectively.[37, 58] The surface of these thin film GSEs shows a higher proportion of N_t compared

to N_d and higher fraction of NBO species. With nitrogen occupying covalent and neutral N_t coordinated positions in the glass network, these additional amounts of N_t nitrogen at the surface must lead to additional NBO species in order to maintain charge balance at the surface of the GSE. This preferential ordering of neutral N_t and NBOs at the GSE surface may lead to a stable passivating solid electrolyte interface (SEI) layer in contact with Na-metal which limits the production of reaction products at the surface of the GSE. However, such a preferential ordering is not observed in the exposed depth of the thin film and as such, this lack of this favorable SEI layer may result in the observation that the depth of the thin film is vulnerable to electrochemical reaction, **Figure 10A**. At this point, however, the cause of the increase in the concentration of these two important species, N_t nitrogen and NBOs, at the surface of the thin film is unknown, but it is being further investigated.

3.7. Electronic Conductivity

With the determination that adverse reactions in the NaPSON-2 thin film GSE were occurring in the bulk of the thin film, the electronic conductivity of the thin film is of interest to determine if a higher than expected electronic conductivity might be enabling these reactions even as the surface of the film remains stable. **Equation 12** relates the driven electronic current, I_t, to the applied voltage, E, and enables the electronic conductivity, σ_e, in $(\Omega cm)^{-1}$ to be determined.[59]

$$\frac{I_t LF}{RTA(1-\exp(-u))} = \sigma_h \exp(u) + \sigma_e \quad (12)$$

$$u = \frac{EF}{RT} \quad (13)$$

Here, L and A are the thickness, in cm, and area, in cm^2, of the sample, respectively, and T the temperature in K. R and F are the gas constant in J mol^{-1} K^{-1} and Faraday's constant in C mol^{-1}. Lastly, u is defined in **Equation 13**, and is the hole conductivity, σ_h, in $(\Omega cm)^{-1}$. In a series of

experiments, the applied voltage, *E*, was held constant and the resulting current was measured until it stabilized, and this limiting stable current was determined. The voltage was then increased and the experiment was repeated. The voltage and resulting current were then used as parameters in **Equation 12**, and plotted in **Figure 16**.

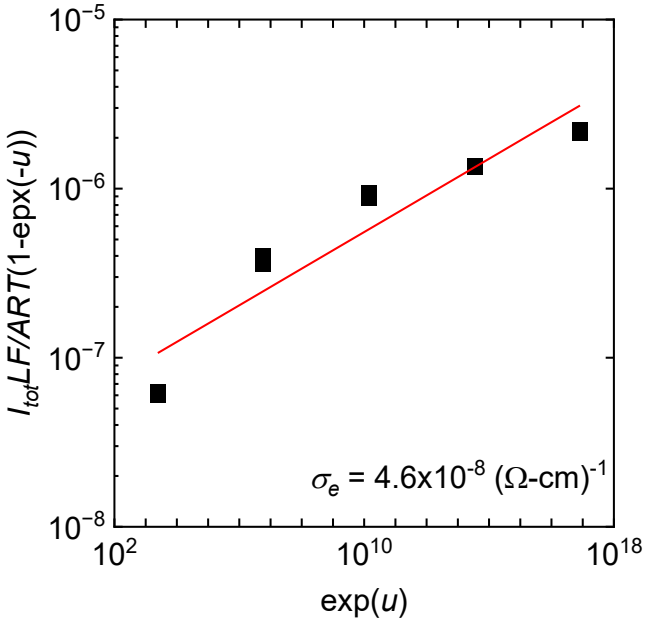

Figure 16: The relationship between current and voltage for the NaPSON-2 thin film, where the intercept represents the electronic conductivity and is shown in the figure for this glass at 25 °C.

The electronic conductivity of the electrolyte was determined from the intercept to be 4.6 x 10^{-8} $(\Omega cm)^{-1}$. The ionic conductivity of the thin film is ~1 x 10^{-6} $(\Omega cm)^{-1}$, leaving less than two orders of magnitude between it and the electronic conductivity. This parasitic electronic conductivity is too high for this electrolyte to be viable in a battery, but also, it could be aiding the electrochemical reactions observed in the bulk of the thin film as described above in section **3.6.**.

3.8. Oxygen's role in electrochemical stability

Oxygen has been shown to improve the electrochemical stability of sulfide solid electrolytes, like in the $Na_3PS_{4-x}O_x$ system, where excellent stability was determined at x = 0.6, which has a S/O ratio of 5.67.[14] However, in the NaPSON-2 GSE reported here, which has a comparable S/(O+N) ratio of 5.27, the GSE appears to be unstable. Added oxygen still improves the stability of these GSEs, which is clear when considering the decomposition behavior of the pure sulfide, $Na_4P_2S_7$, see **Figure S7**, compared to the composition reported here. NaPSON-2 however contains some proportion of $P_2S_7^{4-}$ anions, as well as some PS_4^{3-} anions which form in the glass as a result of a disproportionation reaction[30], leading to instability issues. So, while the S/O ratio is important, engineering the structural units present in GSEs is the key in improving stability.

4. Conclusion

Thin films of a fast sodium ion conducting GSE have been drawn from a new series of NaPSON MOSN glasses. The $\sigma_{d.c.}$ of the NaPSON GSE series was found to generally decrease with increasing *x*, added oxygen and nitrogen, but had significantly higher conductivities compared to their NaPSO counterparts. The $x = 0.2$ GSE in this NaPSON series, NaPSON-2, was observed to be uncrystallizable and yet still had a significant sodium ion conductivity and for this reason, it was chosen as the composition to be drawn into a thin film. When comparing the galvanostatic cycling, the MQ GSE showed little change in the resistance over 100 cycles (450 hours), but the thin film showed an almost three-fold increase in resistance. Despite this, the MQ sample has an order of magnitude higher resistance, making changes in bulk resistance at low current densities due to any decomposition reactions less notable. Based on the reactions that were determined to occur through CV and XPS experiments, it is likely that the changes in resistance

for the MQ material indeed occurred, but perhaps due to the 20 times larger resistance of the MQ material it was less noticeable but could be found at longer times and over a greater number of cycles (>100). The changes in resistance of the thin films are suggested to arise in the bulk of the thin films, where reaction products were observed. Post-cycling XPS measurements showed that the surface of the thin film did not change after contact with Na-metal. The stability of the surface of the thin films was associated with higher concentrations of trigonally N_t nitrogen and NBOs compared to the bulk of the thin film. Reactions in the bulk of the thin film were observed and thought to be exacerbated by a relatively high electronic conductivity of the NaPSON-2 GSE. Future GSE compositions will be optimized to lower the electronic conductivity and avoid pure sulfide $P_2S_7^{4-}$ and PS_4^{3-} anions, which are easily reduced to $P_2S_6^{4-}$ anions and Na_3P, which make the GSE vulnerable to excess, reactive free sulfur.

Supporting Information

Table showing the DSC program used to model the viscosity of NaPSON-2, Arrhenius plot for glasses in the NaPSO series, conductivity values at variable temperatures, activation energies, and pre-exponential factors for all the glasses in NaPSON series, XRD pattern for thin film NaPSON-2, EIS and galvanostatic cycling of MQ NaPSON-2, cycling of thin film NaPSON-2 at 50 μA cm^{-2}, XPS of Na_3P and $Na_4P_2S_7$.

Acknowledgments

Funding for this work was provided by the Iowa Energy Center of the Iowa Department of Economic Development through grant number 307352, by the National Science Foundation through grant DMR 1936913, by the ARPA-E of the Department of Energy through contract numbers DE-AR0000654 and DE-AR-0000778. Additional funding for this work was provided by the Vehicle Technology Office within the Department of Energy though the contract DE-

EE0008852. The authors would like to thank Dapeng “DJ” Jing in the ISU Department of Biotechnology at the Materials Analysis and Research laboratory (MARL) for assistance with XPS measurements.

References

1. Larcher, D.; Tarascon, J. M., Towards greener and more sustainable batteries for electrical energy storage. *Nat Chem* **2015,** *7* (1), 19-29.
2. Gross, M. M.; Percival, S. J.; Lee, R. Y.; Peretti, A. S.; Spoerke, E. D.; Small, L. J., A high-voltage, low-temperature molten sodium battery enabled by metal halide catholyte chemistry. *Cell Reports Physical Science* **2021,** *2* (7).
3. Nikiforidis, G.; van de Sanden, M. C. M.; Tsampas, M. N., High and intermediate temperature sodium-sulfur batteries for energy storage: development, challenges and perspectives. *RSC Adv* **2019,** *9* (10), 5649-5673.
4. Dunn, B.; Kamath, H.; Tarascon, J. M., Electrical energy storage for the grid: a battery of choices. *Science* **2011,** *334* (6058), 928-35.
5. Hueso, K. B.; Palomares, V.; Armand, M.; Rojo, T., Challenges and perspectives on high and intermediate-temperature sodium batteries. *Nano Research* **2017,** *10* (12), 4082-4114.
6. Wittman, R. M.; Perry, M. L.; Lambert, T. N.; Chalamala, B. R.; Preger, Y., Perspective-On the Need for Reliability and Safety Studies of Grid-Scale Aqueous Batteries. *Journal of the Electrochemical Society* **2020,** *167* (9).
7. Rosewater, D.; Williams, A., Analyzing system safety in lithium-ion grid energy storage. *Journal of Power Sources* **2015,** *300*, 460-471.
8. Si, R.-j.; Liu, D.-q.; Xue, S.-q., Experimental Study on Fire and Explosion Suppression of Self-ignition of Lithium Ion Battery. *Procedia Engineering* **2018,** *211*, 629-634.
9. Lee, B.; Paek, E.; Mitlin, D.; Lee, S. W., Sodium Metal Anodes: Emerging Solutions to Dendrite Growth. *Chem Rev* **2019,** *119* (8), 5416-5460.
10. Wang, Y. M.; Song, S. F.; Xu, C. H.; Hu, N.; Molenda, J.; Lu, L., Development of solid-state electrolytes for sodium-ion battery-A short review. *Nano Materials Science* **2019,** *1* (2), 91-100.
11. Ma, Q. L.; Tietz, F., Solid-State Electrolyte Materials for Sodium Batteries: Towards Practical Applications. *Chemelectrochem* **2020,** *7* (13), 2693-2713.
12. Zhao, W.; Yi, J.; He, P.; Zhou, H., Solid-State Electrolytes for Lithium-Ion Batteries: Fundamentals, Challenges and Perspectives. *Electrochemical Energy Reviews* **2019,** *2* (4), 574-605.
13. Manthiram, A.; Yu, X. W.; Wang, S. F., Lithium battery chemistries enabled by solid-state electrolytes. *Nature Reviews Materials* **2017,** *2* (4).
14. Chi, X.; Zhang, Y.; Hao, F.; Kmiec, S.; Dong, H.; Xu, R.; Zhao, K.; Ai, Q.; Terlier, T.; Wang, L.; Zhao, L.; Guo, L.; Lou, J.; Xin, H. L.; Martin, S. W.; Yao, Y., An electrochemically stable homogeneous glassy electrolyte formed at room temperature for all-solid-state sodium batteries. *Nat Commun* **2022,** *13* (1), 2854.
15. Cengiz, M.; Oh, H.; Lee, S. H., Lithium Dendrite Growth Suppression and Ionic Conductivity of Li2S-P2S5-P2O5 Glass Solid Electrolytes Prepared by Mechanical Milling. *Journal of the Electrochemical Society* **2019,** *166* (16), A3997-A4004.

16. Hayashi, A.; Noi, K.; Tanibata, N.; Nagao, M.; Tatsumisago, M., High sodium ion conductivity of glass ceramic electrolytes with cubic Na3PS4. *Journal of Power Sources* **2014,** *258*, 420-423.
17. Aotani, N.; Iwamoto, K.; Takada, K.; Kondo, S., Synthesis and Electrochemical Properties of Lithium Ion Conductive Glass, Li3po4-Li2s-Sis2. *Solid State Ionics* **1994,** *68* (1-2), 35-39.
18. Martin, S. W., Glass and Glass-Ceramic Sulfide and Oxy-Sulfide Solid Electrolytes. In *Handbook of Solid State Batteries, 2nd Edition*, Dudney, N.; West, W.; Nanda, J., Eds. World Scientific: New Jersey, 2015; pp 433-501.
19. Zhao, R.; Hu, G.; Kmiec, S.; Wheaton, J.; Torres III, V. M.; Martin, S. W., Grain-Boundary-Free Glassy Solid Electrolytes based on Sulfide Materials: Effects of Oxygen and Nitrogen Doping on Electrochemical Performance. *Batteries & Supercaps* **2022,** *5* (11), e202100356.
20. Zhao, R.; Hu, G.; Kmiec, S.; Gebhardt, R.; Whale, A.; Wheaton, J.; Martin, S. W., New amorphous oxy-sulfide solid electrolyte material: Anion exchange, electrochemical properties, and lithium dendrite suppression via in situ interfacial modification. *ACS applied materials & interfaces* **2021,** *13* (23), 26841-26852.
21. Kmiec, S.; Olson, M.; Kenney, M.; Martin, S. W., Interpretation of the Na+ Ionic Conductivity in Na4P2S7–xOx Mixed Oxy-Sulfide Glasses: Effects of Oxygen Doping. *Chemistry of Materials* **2022,** *34* (21), 9479-9491.
22. Tsukasaki, H.; Morimoto, H.; Mori, S., Ionic conductivity and thermal stability of Li2O-Li2S-P2S5 oxysulfide glass. *Solid State Ionics* **2020,** *347*.
23. Minami, K.; Mizuno, F.; Hayashi, A.; Tatsumisago, M., Structure and properties of the 70Li2S · (30 −x)P2S5·xP2O5 oxysulfide glasses and glass–ceramics. *Journal of Non-Crystalline Solids* **2008,** *354* (2-9), 370-373.
24. Jha, P. K.; Pandey, O. P.; Singh, K., Structural and thermal properties of Na2S-P2S5 glass and glass ceramics. *Journal of Non-Crystalline Solids* **2013,** *379*, 89-94.
25. Kmiec, S. J.; Lovi, J. M.; Joyce, A.; Bayko, D.; Martin, S. W., Anomalously strong viscosity behavior in mixed oxy-sulfide Na4P2S7-xOx invert glasses. *Journal of Non-Crystalline Solids* **2021,** *553*.
26. Paraschiv, G. L.; Munoz, F.; Jensen, L. R.; Yue, Y. Z.; Smedskjaer, M. M., Structural stability of NaPON glass upon heating in air and nitrogen. *Journal of Non-Crystalline Solids* **2018,** *482*, 137-146.
27. Pilkington, L. A. B., Review Lecture: The float glass process. *Proceedings of the Royal Society of London. A. Mathematical and Physical Sciences* **1997,** *314* (1516), 1-25.
28. Hamilton, L. L., Display innovations through glass. *Japanese Journal of Applied Physics* **2016,** *55* (3S1), 03CA01.
29. Wheaton, J.; Kmiec, S.; Schuler, D.; Sorensen, C.; Martin, S. W., Electrochemical Behavior of Drawn Thin-Film Vitreous Lithium Metaphosphate. *Acs Applied Energy Materials* **2021,** *4* (10), 10835-10842.
30. Olson, M.; Kmiec, S.; Martin, S. W., NaPON Doping of Na4P2S7 Glass and Its Effects on the Structure and Properties of Mixed Oxy-Sulfide-Nitride Phosphate Glass. *Inorg Chem* **2022,** *61* (44), 17469-17484.
31. De Souza, J. E.; Rojas De Souza, S.; Gebhardt, R.; Kmiec, S.; Whale, A.; Warthen Martin, S., LiPON and NaPON glasses: A study of the ammonolysis of lithium and sodium metaphosphate melts. *International Journal of Applied Glass Science* **2019,** *11* (1), 78-86.

32. Mauro, J. C.; Yue, Y.; Ellison, A. J.; Gupta, P. K.; Allan, D. C., Viscosity of glass-forming liquids. *Proc Natl Acad Sci U S A* **2009,** *106* (47), 19780-4.
33. Martin, S. W. Fast Ionic Conduction in Glass: Compositionally Induced Effects on Transport Properties in High Alkali Oxide Glasses (Volumes I and II). Ph.D., Purdue University, Ann Arbor, 1986.
34. Kim, Y.; Saienga, J.; Martin, S. W., Anomalous Ionic Conductivity Increase in Li2S + GeS2 + GeO2 Glasses. *The Journal of Physical Chemistry B* **2006,** *110* (33), 16318-16325.
35. Dudney, N. J.; West, W. C.; Nanda, J., Handbook of Solid State Batteries, 2nd Edition. *Mater Energ* **2016,** *6*, 1-822.
36. Anderson, O. L.; Stuart, D. A., Calculation of Activation Energy of Ionic Conductivity in Silica Glasses by Classical Methods. *Journal of the American Ceramic Society* **1954,** *37* (12), 573-580.
37. Mascaraque, N.; Fierro, J. L. G.; Duran, A.; Munoz, F., An interpretation for the increase of ionic conductivity by nitrogen incorporation in LiPON oxynitride glasses. *Solid State Ionics* **2013,** *233*, 73-79.
38. Kanno, H., A simple derivation of the empirical rule Tg/Tm = 2/3. *J. Non-Cryst. Solids* **1981,** *44* (2-3), 409-13.
39. Sakka, S.; Mackenzie, J. D., Relation Between Apparent Glass Transition Temperature and Liquidus Temperature for Inorganic Glasses. *Journal of Non-Crystalline Solids* **1971,** *6*, 145-162.
40. Zheng, Q. J.; Mauro, J. C.; Ellison, A. J.; Potuzak, M.; Yue, Y. Z., Universality of the high-temperature viscosity limit of silicate liquids. *Physical Review B* **2011,** *83* (21).
41. Zheng, Q. J.; Mauro, J. C.; Yue, Y. Z., Reconciling calorimetric and kinetic fragilities of glass-forming liquids. *Journal of Non-Crystalline Solids* **2017,** *456*, 95-100.
42. Frank Buellesfeld, U. L., Ralf Biertuempfel, Lisa Pudlo, and Helge Jung METHOD FOR PRODUCTION OF GLASS COMPONENTS. 20140342120, 2014.
43. Kmiec, S.; Martin, S. W., Synthesis, Short-Range Order Structure, and Thermal Properties of Mixed Oxy-sulfide Nitride (MOSN) Glasses. *Inorg Chem* **2021,** *60* (18), 13968-13981.
44. Nguyen, H.; Banerjee, A.; Wang, X. F.; Tan, D.; Wu, E. A.; Doux, J. M.; Stephens, R.; Verbist, G.; Meng, Y. S., Single-step synthesis of highly conductive Na3PS4 solid electrolyte for sodium all solid-state batteries. *Journal of Power Sources* **2019,** *435*.
45. Wolfgang Brocknera, B. J., Frank Menzela, Vidar Remi Jensenb, Martin Ystenesb, Vibrational spectra and ab initio quantum mechanical calculation of energy, geometry and vibrational frequencies of the oxothiophosphate ions P03S3-, PO2S23- and POS33-. *Journal of Molecular Structure* **1993**.
46. Kmiec, S.; Joyce, A.; Bayko, D.; Martin, S. W., Glass formation and structure of melt quenched mixed oxy-sulfide Na4P2S7-xOx glasses for $0 \leq x \leq 5$. *Journal of Non-Crystalline Solids* **2020,** *534*.
47. El Jaroudi, O.; Picquenard, E.; Gobeltz, N.; Demortier, A.; Corset, J., Raman Spectroscopy Study of the Reaction between Sodium Sulfide or Disulfide and Sulfur: Identity of the Species Formed in Solid and Liquid Phases. *Inorg Chem* **1999,** *38* (12), 2917-2923.
48. Jha, P. K.; Pandey, O. P.; Singh, K., FTIR spectral analysis and mechanical properties of sodium phosphate glass-ceramics. *Journal of Molecular Structure* **2015,** *1083*, 278-285.
49. Moustafa, Y. M.; El-Egili, K., Infrared spectra of sodium phosphate glasses. *Journal of Non-Crystalline Solids* **1998,** *240* (1-3), 144-153.

50. Wang, M. J.; Choudhury, R.; Sakamoto, J., Characterizing the Li-Solid-Electrolyte Interface Dynamics as a Function of Stack Pressure and Current Density. *Joule* **2019,** *3* (9), 2165-2178.
51. Minami, T.; Hayashi, A.; Tatsumisago, M., Preparation and characterization of lithium ion-conducting oxysulfide glasses. *Solid State Ionics* **2000,** *136*, 1015-1023.
52. Hayashi, A.; Tatsumisago, M.; Minami, T.; Miura, Y., Structural Investigation of 95(0.6Li2S0.4SiS2)5Li4SiO4 Oxysulfide Glass by Using X-ray Photoelectron Spectroscopy. *Journal of the American Ceramic Society* **2005,** *81* (5), 1305-1309.
53. Fantauzzi, M.; Elsener, B.; Atzei, D.; Rigoldi, A.; Rossi, A., Exploiting XPS for the identification of sulfides and polysulfides. *Rsc Advances* **2015,** *5* (93), 75953-75963.
54. Liu, Z.; Borodin, A.; Li, G.; Liu, X.; Li, Y.; Endres, F., X-ray Photoelectron Spectroscopy Probing of the Interphase between Solid-State Sulfide Electrolytes and a Lithium Anode. *The Journal of Physical Chemistry C* **2019,** *124* (1), 300-308.
55. Hartley, G. O.; Jin, L.; Bergner, B. J.; Jolly, D. S.; Rees, G. J.; Zekoll, S.; Ning, Z.; Pateman, A. T. R.; Holc, C.; Adamson, P.; Bruce, P. G., Is Nitrogen Present in Li3N·P2S5 Solid Electrolytes Produced by Ball Milling? *Chemistry of Materials* **2019,** *31* (24), 9993-10001.
56. Ruan, Y.; Lu, Y.; Huang, X.; Su, J.; Sun, C.; Jin, J.; Wen, Z., Acid induced conversion towards a robust and lithiophilic interface for Li–Li7La3Zr2O12 solid-state batteries. *Journal of Materials Chemistry A* **2019,** *7* (24), 14565-14574.
57. Lazar, M.; Kmiec, S.; Joyce, A.; Martin, S. W., Investigations into Reactions between Sodium Metal and Na3PS4-xOx Solid-State Electrolytes: Enhanced Stability of the Na3PS3O Solid-State Electrolyte. *Acs Applied Energy Materials* **2020,** *3* (12), 11559-11569.
58. Marchand, R.; Agliz, D.; Boukbir, L.; Quemerais, A., Characterization of nitrogen containing phosphate glasses by X-ray photoelectron spectroscopy. *Journal of Non-Crystalline Solids* **1988,** *103* (1), 35-44.
59. Huggins, R. A., Simple method to determine electronic and ionic components of the conductivity in mixed conductors a review. *Ionics* **2002,** *8* (3), 300-313.

TOC Graphic:

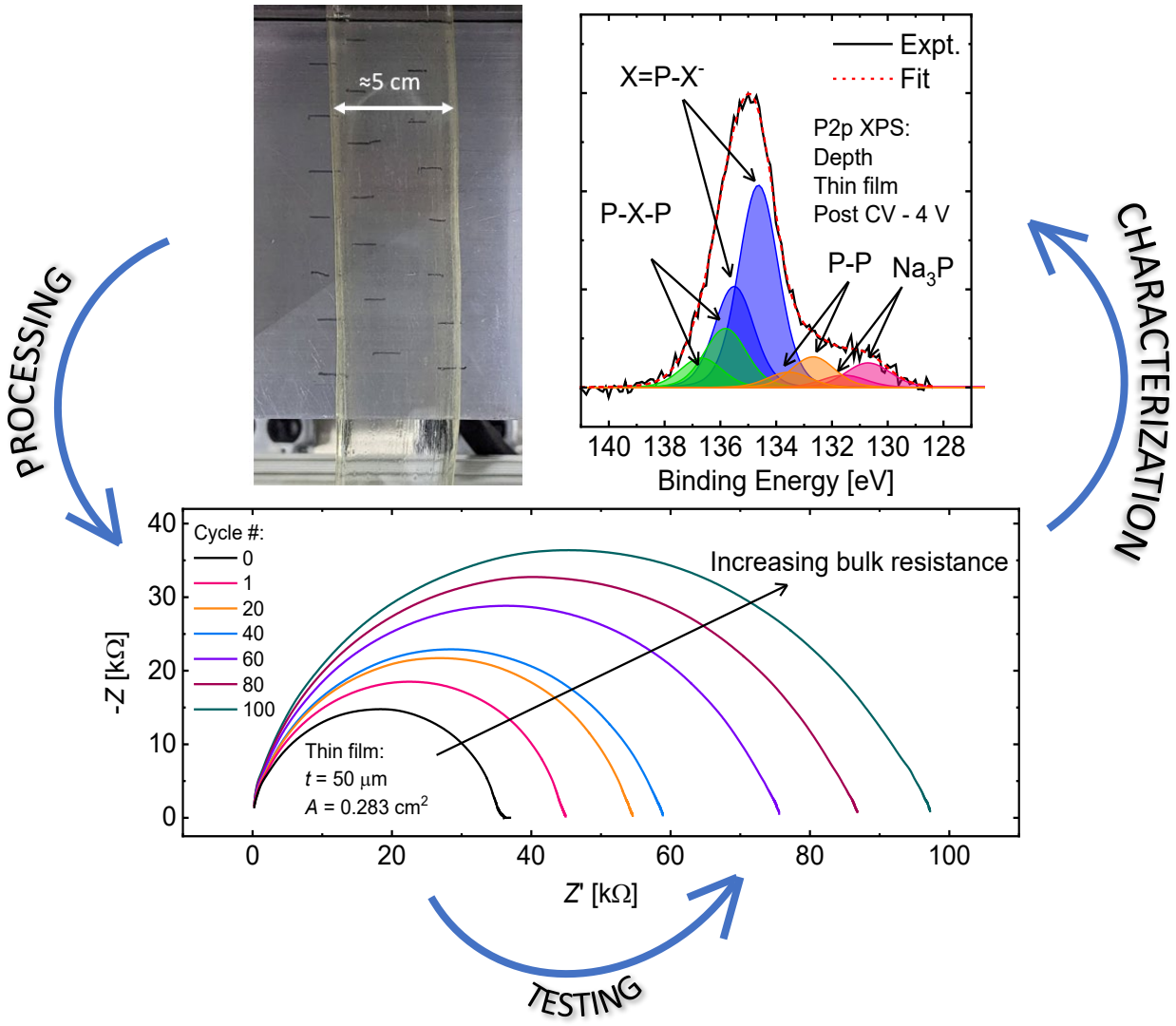
PROCESSING
≈5 cm
X=P-X⁻
Expt.
Fit
P2p XPS:
Depth
Thin film
Post CV - 4 V
P-X-P
P-P
Na3P
140 138 136 134 132 130 128
Binding Energy [eV]
CHARACTERIZATION
Cycle #:
0
1
20
40
60
80
100
Increasing bulk resistance
Thin film:
t = 50 μm
A = 0.283 cm2
-Z [kΩ]
Z' [kΩ]
0
10
20
30
40
0
20
40
60
80
100
TESTING